Hybrid III–V Nanowire and Perovskite Architectures for Advanced Multi-Junction Solar Cells

MATTEO TIRRITO
DEPARTMENT OF PHYSICS | FACULTY OF ENGINEERING | LUND UNIVERSITY

Hybrid III–V Nanowire and Perovskite Architectures for Advanced Multi-Junction Solar Cells

Hybrid III–V Nanowire and Perovskite Architectures for Advanced Multi-Junction Solar Cells

by Matteo Tirrito

LUND
UNIVERSITY

Thesis for the degree of Doctor of Philosophy

To be presented, with the permission of the Faculty of Engineering at Lund University, for public criticism in the Rydberg lecture hall (Rydbergsalen) at the Department of Physics on Wednesday, the 13th of May 2026 at 13:15.

Thesis advisor
Professor Magnus T. Borgström

Supporting advisors
Professor Eva Unger

Faculty opponent
Professor Thomas Hannappel
TU Ilmenau, Germany

Organization
LUND UNIVERSITY

Department of Physics
Box 118
SE–221 00 LUND
Sweden

Document name
DOCTORAL DISSERTATION

Date of disputation
2026-05-13

Sponsoring organization

Author(s)
Matteo Tirrito

Title and subtitle
Hybrid III–V Nanowire and Perovskite Architectures for Advanced Multi-Junction Solar Cells

Abstract
Next-generation photovoltaic technologies must achieve high efficiency, use less material, and allow scalable manufacturing. This study investigates III–V semiconductor nanowires for advanced solar cells and examines their integration with metal–halide perovskites for hybrid multi-junction devices.

III–V nanowires were grown by Au-assisted vapor–liquid–solid epitaxy, with growth optimization of GaAs, InP, and GaInP revealing the effects of precursors flow, temperature, and V/III ratio on nanowire structure and heterostructure quality. GaInP/InP tandem-junction nanowires were then fabricated and characterized. Electron-beam-induced current microscopy refined junction placement and doping, while processed devices demonstrated voltage addition and confirmed stacked device operation. However, quantum efficiency characterisation showed that the GaInP top cell is the current bottleneck, indicating a need for better surface passivation.

To integrate III–V nanowires with perovskites, the optical properties of hybrid structures were studied to determine fabrication needs for efficient absorption. Simulations quantified absorption and photocurrent generation in pure and hybrid nanowire geometries, highlighting the importance of optical resonances, material choice, and geometry for efficient multi-junction operation and guiding absorber structure design.

Guided by these results, hybrid perovskite/III–V nanowire films were fabricated using solution-based methods, such as inkjet printing and spin-on patterning. These enable perovskite infiltration into nanowire arrays at low temperatures on large areas, maintaining strong optical coupling. Although performance is still limited by interface quality and perovskite stability, the hybrid architecture is a promising route for scalable, lightweight, and low-material photovoltaics.

Overall, the combined efforts in nanowire growth, monitoring, optical modeling, device processing, and hybrid integration establish a scalable path for high-efficiency nanowire-based photovoltaics.

Key words
III-V nanowires, perovskite, multi-junction solar cells, InP, GaAs.

Classification system and/or index terms (if any)

Supplementary bibliographical information

Language
English

ISSN and key title

ISBN
978-91-8104-988-6 (print)
978-91-8104-989-3 (pdf)

Recipient's notes

Number of pages
145

Price

Security classification

Signature _____ Date 26-04-16

Hybrid III–V Nanowire and Perovskite Architectures for Advanced Multi-Junction Solar Cells

by Matteo Tirrito

LUND
UNIVERSITY

Division of Solid State Physics
Department of Physics
Faculty of Engineering
Lund University

Department of Physics
Faculty of Engineering
Lund University

Box 118
SE–221 00 LUND
Sweden

ISBN: 978-91-8104-988-6 (print)
ISBN: 978-91-8104-989-3 (pdf)

Printed in Sweden by Media-Tryck, Lund University, Lund 2026

to Liam Rinaldi Shokri

Contents

List of publications

This thesis is based on the following publications:

I **Vertically Processed GaInP/InP Tandem-Junction Nanowire Solar Cells**
D. Alcer, **M. Tirrito**, L. Hrachowina, and Magnus T. Borgström
ACS Applied Nano Materials 7, p. 2352–2358 (2024)

I was responsible for the characterization of the nanowires by measuring the electron beam induced current. I contributed to the writing of the paper.

II **Optical Analysis of Perovskite III-V Nanowires Interpenetrated Tandem Solar Cells**
M. Tirrito, P. Manley, C. Becker, E. Unger, and M. T. Borgström
Nanomaterials 14(6), p. 518–528 (2024)

I was the main responsible for developing the optical model, designing the mesh and the parameters of interests. This involved both analytical and numerical calculations by means of JMCsuite software. I was the main responsible for writing the article.

III **GaAs NW array growth over a large parameter space**

M. Tirrito, J. E. Escobar, E. B. Montañés and Magnus T. Borgström
Manuscript to be submitted (2026)

I was the main responsible for the growth of the semiconductor material. This involved writing the recipe and designing the variation of the precursors flow. I was the main responsible for writing the article.

All papers are reproduced with permission of their respective publishers.

Acknowledgements

I am deeply grateful to my supervisor, Prof. Borgström, for his guidance, patience, and the countless hours we spent working side by side in the lab. His generosity in sharing his scientific knowledge and, above all, his belief in this project during the most difficult moments made the difference. I also warmly thank my co-supervisor, Prof. Unger, for her expertise and broad scientific network, which enabled our modelling work, as well as Prof. Becker and Dr. Manley for their continued encouragement and support.

I would like to thank the colleagues with whom I shared these years, and without whom this journey still would not have been the same. In particular, I am grateful to Dr. Escobar for sharing the joy and curiosity that are the true salt of science; to Dr. Zhao, from whom I learned so much and who has been the best colleague I could have wished for; to Dr. Hrachowina for the long evenings spent patiently training me and for his thoughtful advice; and to Dr. Alcer for his infinite kindness. I also thank all past and present group members, including Dr. Adham, Shcherbakova, Zhu, and Chen, for contributing to a stimulating and supportive working environment.

I would also like to acknowledge the technical staff who make our research possible, especially Dr. Lehmann, whose dedication and ethical standards are a constant example of what good science is, and Kvennefors, whose professionalism and infinite knowledge have repeatedly sparked new ideas and deeper understanding.

This work was carried out at NanoLund, Lund University. Financial support was provided by Myfab, the Swedish Energy Agency, the Wallenberg Initiative Materials Science for Sustainability (WISE), the Knut and Alice Wallenberg Foundation, and the European Union's Horizon 2020 research and innovation programme under the Marie Skłodowska-Curie Grant Agreement No. 945378.

Finally, my deepest gratitude goes to my family and friends, whose support, patience, and understanding have been priceless. Their care has created a debt I can never fully repay, but to which I owe my unconditional loyalty and love. While I cannot say whether I could have completed this work without them, I know that their presence gave these years their true meaning, turning them into cherished memories. They were the teaspoon of sugar in the coffee: making bitterness a flavour to enjoy.


myfab
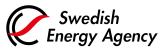
Swedish
Energy Agency

Knut and Alice
Wallenberg
Foundation


Abstract

Next-generation photovoltaic technologies must achieve high efficiency, use less material, and allow scalable manufacturing. This study investigates III–V semiconductor nanowires for advanced solar cells and examines their integration with metal–halide perovskites for hybrid multi-junction devices.

III–V nanowires were grown by Au-assisted vapor–liquid–solid epitaxy, with growth optimization of GaAs, InP, and GaInP revealing the effects of precursors flow, temperature, and V/III ratio on nanowire structure and heterostructure quality. GaInP/InP tandem-junction nanowires were then fabricated and characterized. Electron-beam-induced current microscopy refined junction placement and doping, while processed devices demonstrated voltage addition and confirmed stacked device operation. However, quantum efficiency characterisation showed that the GaInP top cell is the current bottleneck, indicating a need for better surface passivation.

To integrate III–V nanowires with perovskites, the optical properties of hybrid structures were studied to determine fabrication needs for efficient absorption. Simulations quantified absorption and photocurrent generation in pure and hybrid nanowire geometries, highlighting the importance of optical resonances, material choice, and geometry for efficient multi-junction operation and guiding absorber structure design.

Guided by these results, hybrid perovskite/III–V nanowire films were fabricated using solution-based methods, such as inkjet printing and spin-on patterning. These enable perovskite infiltration into nanowire arrays at low temperatures on large areas, maintaining strong optical coupling. Although performance is still limited by interface quality and perovskite stability, the hybrid architecture is a promising route for scalable, lightweight, and low-material photovoltaics.

Overall, the combined efforts in nanowire growth, monitoring, optical modeling, device processing, and hybrid integration establish a scalable path for high-efficiency nanowire-based photovoltaics.

Popular science summary

Solar energy has the potential to power a wide range of applications, including residential, industrial, and data center operations, with high efficiency and affordability. Although current solar panels are essential for renewable energy generation, even the most advanced commercial devices capture only a fraction of incident sunlight. This limitation arises because individual solar cells absorb only specific wavelengths of light. Tandem solar cells, which stack multiple light-absorbing materials so that each layer harvests a distinct portion of the solar spectrum, offer a promising solution. This approach reduces energy losses and can increase efficiency beyond the limits of conventional silicon-based technology.

This thesis investigates a novel approach to tandem photovoltaics that integrates two advanced materials: III–V semiconductor nanowires and perovskites.

III–V nanowires are extremely thin, needle-like crystals that are thousands of times slimmer than a human hair. Despite covering only a small fraction of a surface, their geometry enables efficient light trapping and concentration. These structures inherently minimize light reflection and can be engineered to form multiple junctions within each nanowire. Due to their minimal material requirements, nanowires offer the potential for high performance at significantly reduced cost compared to traditional III–V devices.

In contrast, perovskites are lightweight, tunable, and cost-effective materials that have significantly advanced the field of photovoltaics. They demonstrate high efficiency in converting light to electricity and can be processed using low-temperature, scalable techniques such as solution processing and inkjet printing. The bandgap of perovskites can be readily adjusted through chemical composition, making them suitable partners for integration with nanowire-based devices.

This work leverages the limited surface area occupied by nanowires as a template for perovskite deposition. In this design, perovskite material is deposited around and between arrays of III–V nanowires. The resulting structure, referred to as an interpenetrated nanowire–perovskite tandem architecture, is designed to:

- capture a greater proportion of sunlight while minimizing material usage,

- combine the high performance of III–V absorbers with the cost-effectiveness of perovskites, and
- exploit the intrinsic anti-reflection and light-trapping properties of nanowires.

To investigate this concept, the thesis examines both the optical behavior of hybrid tandem structures and the growth and fabrication of III–V nanowire arrays suitable for advanced solar cell architectures. Optical modeling elucidates the mechanisms of light absorption, reflection, and loss within these complex three-dimensional geometries, guiding the optimization of material thicknesses and interfaces. Concurrently, studies on nanowire growth assess how parameters such as precursor flow rates, temperature, and surface chemistry influence the morphology and crystal quality of GaAs and InP nanowires.

Although conventional III–V solar cells are currently too expensive for widespread terrestrial deployment, integrating nanowires with perovskites in this novel geometry presents a pathway toward high-efficiency, lightweight, and potentially cost-effective tandem devices. In addition to enhanced efficiency, this research identifies new manufacturing opportunities, including inkjet-printed contacts and scalable deposition methods compatible with sensitive materials.

In summary, this thesis provides new insights into the optical behavior of hybrid nanowire–perovskite systems and the effective synthesis and optimization of these structures. The findings contribute to the development of future tandem solar cells that can achieve high efficiency while remaining compatible with scalable and cost-effective production methods.

List of abbreviations

ALD Atomic Layer Deposition

AM1.5G Air Mass 1.5 Global solar spectrum

AsH_3 Arsine

BCB Benzocyclobutene

Br Bromine (in perovskites)

CVD Chemical Vapour Deposition

DEZn Diethylzinc

DMD Digital Micromirror Device

EBIC Electron-Beam-Induced Current

EQE External Quantum Efficiency

ETL Electron Transport Layer

Epison Acoustic/ultrasonic precursor monitoring system

FF Fill Factor

GaAs Gallium Arsenide

GaInP Gallium Indium Phosphide

H_2S Hydrogen Sulphide

HCl Hydrogen Chloride

HTL Hole Transport Layer

InP Indium Phosphide

ITO Indium Tin Oxide

J_{SC} Short-Circuit Current Density

LED Light Emitting Diode (in SEM nanoprobe context)

LiF Lithium Fluoride

$MAPbBr_3$ Methylammonium Lead Bromide

$MAPb(I_{1-x}Br_x)_3$ Mixed-halide perovskite absorber

MLA Mask-less Lithography Apparatus

MHP Metal-Halide Perovskite

MOVPE Metalorganic Vapour Phase Epitaxy

MPP Maximum Power Point

NW Nanowire

PH_3 Phosphine

PL Photoluminescence

PLQY Photoluminescence Quantum Yield

PMGI Polydimethylglutarimide (undercut resist)

PO_x Phosphorus-oxide species (surface)

PV Photovoltaics

RHEED Reflection High-Energy Electron Diffraction

SAM Self-Assembled Monolayer

SEM Scanning Electron Microscopy

SiO_x Silicon Oxide (non-stoichiometric)

SIR Spatial light modulation (see SLM)

SLM Spatial Light Modulator

Spiro-OMeTAD Organic hole transport material (Spiro-methoxy-OMeTAD)

STEM Scanning Transmission Electron Microscopy

TBAs Tertiarybutylarsine

TBP Tertiarybutylphosphine

TDL Talbot Displacement Lithography

TEGa Triethylgallium

TESn Tetraethyltin

TMAl Trimethylaluminium

TMGa Trimethylgallium

TMIn Trimethylindium

TMI Trimethylindium (older notation in InP literature)

TCO Transparent Conductive Oxide

TSL Twinning Superlattice

TPL Triple-Phase Line

V/III Group-V / Group-III precursor ratio

VLS Vapour–Liquid–Solid (growth mechanism)

$\boldsymbol{V_{OC}}$ Open-Circuit Voltage

WZ Wurtzite crystal phase

XEOL X-ray Excited Optical Luminescence

XRD X-Ray Diffraction

ZB Zincblende crystal phase

1 | Introduction

Electricity has become the foundation of contemporary energy systems. In 2024, global electricity consumption rose by 4.3%, primarily due to heatwaves, accelerated electrification in transportation and buildings, and the proliferation of data centres [1]. The International Energy Agency (IEA) reports that electricity consumption increased by 1,080 TWh in 2024 alone, nearly double the average annual growth observed over the previous decade [1]. In response, policymakers at COP28 committed to tripling renewable capacity by 2030. However, even the most optimistic deployment scenarios suggest that meeting demand while reducing emissions will require both large-scale expansion and significant device-level efficiency improvements in photovoltaics (PV) [2].

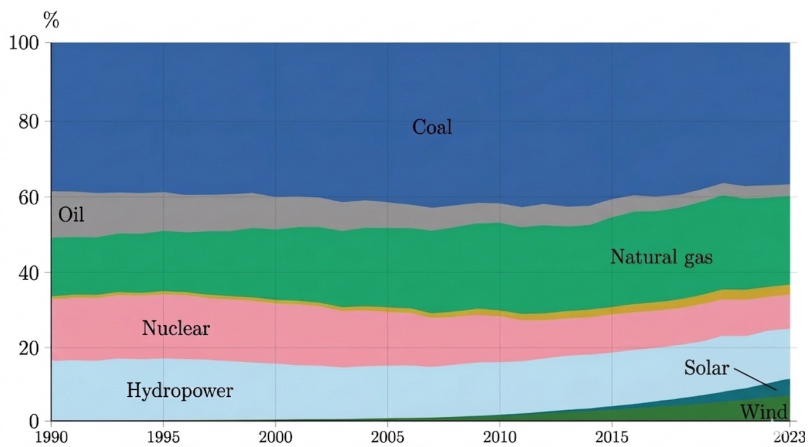

Figure 1.1: Global electricity consumption chart from 1990–2023. Reproduced from [3].

In this context, photovoltaics (PV) are particularly well positioned due to their modularity, scalability, declining costs, and suitability for deployment across utility, commercial, and building-integrated applications [4, 5], as reflected in the rapid rise of solar generation shown in Figure 1.1. However, the market's leading technology, single-junction crystalline silicon, is approaching its theoretical efficiency limit. As of 2025, the highest laboratory efficiency for crystalline silicon solar cells reached **27.81%** (LONGi HIBC architecture, certified by ISFH) [6], and the highest commercially available silicon module efficiency is **25.4%** (LONGi HPBC 2.0, certified by Fraunhofer ISE) [7]. While new concepts like interdigitated back contacts, and PERC has led to advances in passivation and light management continue to enhance silicon performance, the power that can be extracted from single-bandgap absorbers is ultimately limited by fundamental loss mechanisms, intrinsic to the solar spectrum, as shown in Figure 1.2a. High-energy photons rapidly thermalise to the band edge, while sub-bandgap photons are not absorbed. Additional radiative and entropic losses, including emission losses, Boltzmann losses associated with entropy generation, and the Carnot limit on extractable work, further restrict the achievable voltage, as illustrated in Figure 1.2b. Collectively, these factors establish the Shockley–Queisser limit, which places the maximum efficiency of a single-junction cell near $\sim 33\%$ for band gaps in the range of 1.1–1.4 eV [8].

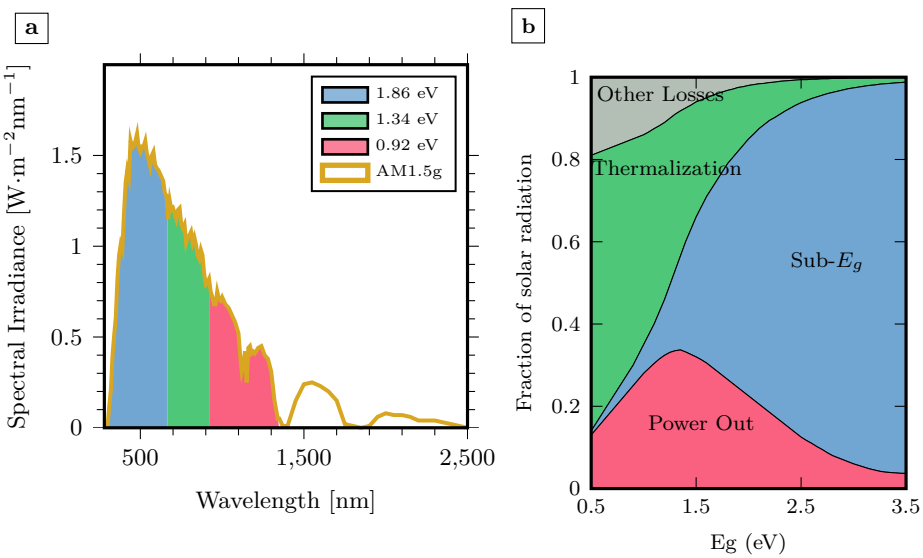

Figure 1.2: (a) Spectral irradiance of the ground solar spectrum (AM1.5g), partitioned by different E_g absorbers. (b) Detailed balance and losses as a function of the bandgap E_g. Adapted from [9].

These intrinsic limitations motivate the development of multi-junction (MJ) architectures, which divide the solar spectrum among multiple subcells to mitigate both thermalisation and sub-bandgap transmission losses as detailed in Figure 1.2b. By assigning high-energy photons to wide-bandgap top absorbers and transmitting lower-energy photons to successively narrower-bandgap junctions, MJ devices implement spectral splitting to reduce entropy generation and boost the voltage of each subcell, enabling efficiencies far beyond the single-junction limit [10].

Planar III–V multi-junction cells have set the efficiency benchmark for decades, consistently pushing the one-sun record beyond 40% through bandgap engineering, high radiative efficiency, and low non-radiative recombination [11, 12]. The best certified one-sun III–V multi-junction efficiency is **39.5%** [12, 13], while under concentrated illumination, four-junction devices have achieved **47.6%** at 665 suns [13, 14]. Their terrestrial deployment, however, remains limited by epitaxial growth costs, expensive substrates (e.g. GaAs, Ge), and complex metallisation and interconnection schemes, nonetheless the lenses needed for concentrated PV increase the modules cost and complexity.

1.1 Perovskite

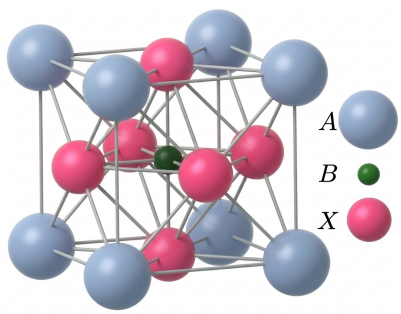

Figure 1.3: Perovskite pseudo-cubic crystal structure, A is the monovalent cation, B the divalent cation, and X the halide.

Metal-halide perovskites (MHPs), whose crystal structure is depicted in Figure 1.3, have significantly impacted the PV research field by combining direct band gaps, strong absorption, long carrier diffusion lengths, and relatively benign defect physics with low-temperature, solution-compatible processing [15–17]. Perovskite single-junction efficiencies, initially reported by Kojima et al. at 3.5% [18], have exceeded 25% within just over a decade [13, 19–21]. Notably, their bandgap is compositionally tunable across approximately 1.2–2.4 eV, facilitating their

application as top or middle absorbers optimised for current matching in tandem devices [16, 22, 23]. Persistent challenges include environmental sensitivity (moisture and oxygen), thermal stress [24], ion migration, and mixed-halide phase segregation in wide-bandgap compositions [25]. Nevertheless, ongoing advancements in interface engineering, solvent- or vapour-assisted crystallisation, and additive strategies have enhanced both performance and stability [23, 26, 27]. Concurrently, digital and additive manufacturing techniques such as inkjet printing have advanced, enabling mask-free patterning, high material utilisation, and compatibility with roll-to-roll processing [28, 29].

These scientific advancements have already facilitated initial industrial deployments. In 2024, Oxford PV completed the first commercial sale of perovskite–silicon tandem modules, achieving module efficiencies of **24.5%** and a laboratory record of **26.9%** for its perovskite-on-silicon tandem architecture [13, 30]. Simultaneously, LONGi demonstrated industrial-scale progress in perovskite–silicon tandem technology, achieving a world-record certified efficiency of **34.85%** for a two-terminal tandem device in 2025 [31]. These milestones underscore the rapid transition of perovskite-based tandem technologies from laboratory demonstrations to scalable industrial products.

1.2 III–V nanowires

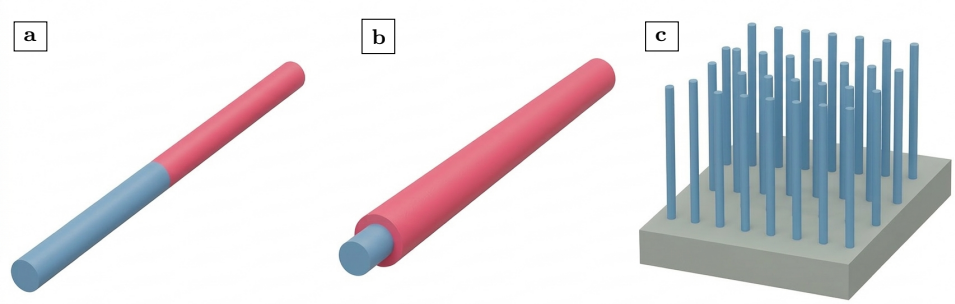

Figure 1.4: Schematics of typical bottom-up grown nanowires. (a) Axial nanowires. (b) Core-shell radial nanowires. (c) Nanowire arrays.

III–V nanowires (NWs) represent an alternative approach to achieving high-efficiency and potentially scalable photovoltaics. Their subwavelength geometry enables wave-optical resonances, Mie-type scattering, and angular redistribution, collectively enhancing absorption beyond the geometric fill factor [32–34]. Radial strain relaxation allows for lattice-mismatched material combinations that are

difficult to achieve in planar heteroepitaxy, while both axial and radial junction designs can decouple absorption and collection, thereby reducing minority-carrier path lengths [35, 36]. State-of-the-art NW devices have demonstrated high external quantum efficiencies and open-circuit voltages. Furthermore, axially stacked multi-junctions within a single NW, such as GaInP/InP and GaInP/InP/InAsP, have been realised, including the integration of Esaki tunnel diodes [37, 38]. However, device-level challenges remain: high sidewall-to-volume ratios increase surface recombination unless interfaces are effectively passivated; array uniformity (diameter, pitch, height) influences spectral selectivity and current matching; and conformal, low-resistance contacts on 3D topographies require process adaptations beyond those used for the planar counterparts [39–41].

1.3 Manufacturability: contacts and scalable deposition

Bridging the gap between laboratory-scale devices and manufacturable technologies necessitates innovations focused on cost reduction. Recent research into cost levers—including substrate reuse, alternative epitaxy, and scalable metallisation—has demonstrated significant potential [42, 43]. Notably, *mask-and-plate* metallisation has been demonstrated on III–V/Si triple-junction cells, where inkjet-defined plating resist guides electroplated nickel to form narrow, uniform fingers, thereby replacing costly photolithography without sacrificing efficiency (31.6% AM1.5G on a 4 cm^2 device) [44]. In parallel, NREL's III–V programme has shown that integrating alternative epitaxy routes, substrate reuse, and advanced contact design can reduce costs while maintaining high power conversion efficiency [45]. Nevertheless, terrestrial deployment remains largely limited to niche, area-constrained applications where absolute efficiency is prioritised over cost [11, 45].

For perovskites, the manufacturing question centres on process windows that deliver dense, low-defect films at low temperature across large areas. Inkjet printing addresses patterning and materials utilisation while remaining compatible with multi-layer stacks and selective deposition; still, print-head reliability, ink rheology, coffee-ring suppression and interlayer wetting must be engineered together to avoid pinholes and non-uniform thickness [28]. Solvent-vapour and hybrid annealing strategies complement deposition by extending nucleation windows and enabling Ostwald ripening, which increases grain size and reduces trap densities without aggressive thermal budgets, critical for flexible substrates and

for integration atop temperature-sensitive bottom cells [46].

1.3.1 A hybrid opportunity: perovskites on III–V nanowires

Integrating perovskites with III–V nanowire (NW) architectures seeks to combine the spectral tunability and low-temperature processing advantages of MHPs with the advanced light-management and high-voltage potential of III–V absorbers. Nanophotonic concepts developed for perovskites, including photonic crystals and metasurfaces that optimise absorption and emission while reducing parasitic losses, offer design flexibility for interpenetrated geometries in which perovskites are deposited around and between NWs [47, 48]. In this configuration, the NW array functions as an intrinsic anti-reflection and light-trapping medium, utilising only a fraction of the III–V material [34]. Key integration challenges include: (i) achieving conformal perovskite infiltration or coating in high-aspect-ratio arrays without voids or passivation damage; (ii) ensuring chemically and electronically benign interfaces to prevent Fermi-level pinning and non-radiative losses at the III–V/MHP interface; (iii) developing front-contact schemes with low series resistance and minimal optical shading on three-dimensional surfaces; and (iv) maintaining reliability under thermal cycling, damp heat, and ultraviolet (UV) exposure, with encapsulation methods compatible with additive manufacturing [26, 27, 44].

1.4 Outline

This thesis investigates III–V NW and their integration with perovskites for tandem application through two complementary approaches. First, optical modelling is developed and applied to interpenetrated tandem designs that leverage the compact footprint of NW arrays, quantifying reflectivity, parasitic absorption, and current matching in both two-terminal and three-terminal configurations. Second, the fabrication and growth parameter space of III–V NW arrays suitable for advanced PV, including axial multijunction integration and evaluation of process levers. Together, these studies aim to advance the understanding of hybrid NW–perovskite tandems and to identify pathways toward high-performance, scalable multijunction solar cells. The thesis is developed in the following chapters:

- **Chapter 2: Theoretical Background**
  Introduces the fundamentals of p–n junction operation, recombination and

transport, and the principles behind multi-junction solar cells, providing the theoretical framework used throughout the thesis.

- **Chapter 3: Methods**
  Describes the experimental and modelling tools employed in this work, including MOVPE nanowire growth, lithography and processing steps, perovskite deposition, and the optical modelling approach.

- **Chapter 4: Processing and Characterisation**
  Presents the fabrication of nanowire and hybrid devices, together with the electrical, optical, and structural characterisation techniques used to evaluate junction quality and device performance.

- **Chapter 5: Summary and Results**
  Summarises the main findings of the three studies: growth optimisation of GaAs nanowires, optical modelling of nanowire–perovskite tandems, and electrical analysis of GaInP/InP tandem nanowires.

- **Chapter 6: Conclusions and Outlook**
  Highlights the key insights gained and outlines the remaining challenges and future opportunities for advancing III–V nanowire and hybrid perovskite–nanowire multi-junction photovoltaics.

2 | Theoretical Background

2.1 Working principle of the p–n junction

A p–n junction is the canonical solid-state structure used to separate and collect photogenerated carriers in a solar cell. The p region is prepared such that the equilibrium hole density satisfies $p \gg n$, while in the n region the equilibrium electron density satisfies $n \gg p$. The gradient in carrier concentration drives the diffusion of majority carriers across the interface, where they become minority carriers on the opposite side. The fixed ionised substitutional dopants form a space charge region that establishes an internal electric field in a depletion region around the junction; far from the interface, charge neutrality is restored. Under illumination, electron–hole pairs are generated in the absorber. Efficient operation requires suppressing minority-carrier flow to the wrong terminal while extracting majority carriers with minimal loss; this selectivity is achieved by doping and the use of thin, selective-transport layers at the contacts.

2.1.1 Equilibrium band diagram

At thermal equilibrium, there is no net current, and the Fermi level E_F is spatially constant as shown in Figure 2.1. In the nondegenerate limit, the carrier densities follow Boltzmann statistics:

$$n = N_C \exp\left(-\frac{E_C - E_F}{k_B T}\right), \qquad p = N_V \exp\left(-\frac{E_F - E_V}{k_B T}\right), \tag{2.1}$$

where N_C and N_V are the effective densities of states, k_B is Boltzmann's constant, and T is the absolute temperature; the mass–action law holds, $np = n_i^2$ with n_i the intrinsic carrier density. For an abrupt homojunction, the built-in (diffusion) potential is

$$qV_{bi} = k_B T \ln\left(\frac{N_A N_D}{n_i^2}\right), \tag{2.2}$$

with q the elementary charge and N_A, N_D the acceptor and donor concentrations. Within the depletion approximation, the space charge is attributed solely to ionised dopants.

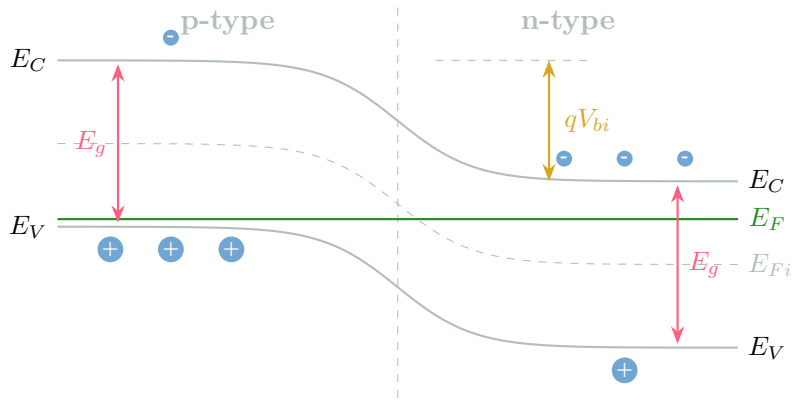

Figure 2.1: Energy-band diagram of a p–n junction at thermal equilibrium. The conduction band E_C, valence band E_V, and Fermi level E_F are shown; E_F is constant in equilibrium. Dashed lines indicate the intrinsic level E_{Fi} in the p and n regions. Band bending across the depletion region gives the built-in electrostatic potential qV_{bi}.

Charge neutrality implies that:

$$N_A w_{Dp} = N_D w_{Dn}, \tag{2.3}$$

where w_{Dp} and w_{Dn} are the depletion widths extending into the p and n sides, respectively. The electrostatic potential profile across the depletion region follows from Poisson's equation,

$$-\frac{d}{dx}\left(\frac{d\phi}{dx}\right) = \frac{\rho(x)}{\varepsilon_s} = \frac{q}{\varepsilon_s}[N_D(x) - n(x) - N_A(x) + p(x)], \tag{2.4}$$

and, within the depletion approximation, $\rho(x) \simeq +qN_A$ on the p side and $\rho(x) \simeq -qN_D$ on the n side. Integrating Poisson's equation over the depletion region relates the total depletion width $W = w_{Dp} + w_{Dn}$ to potential drop $(V_{bi} - V)$, yielding:

$$W = w_{Dp} + w_{Dn} = \sqrt{\frac{2\varepsilon_s}{q}\left(\frac{1}{N_A} + \frac{1}{N_D}\right)(V_{bi} - V)}, \tag{2.5}$$

with $\varepsilon_s = \varepsilon_r \varepsilon_0$ the semiconductor permittivity, ε_r the relative permittivity, ε_0 the vacuum permittivity, and V the applied voltage; reverse bias ($V < 0$) increases W, while forward bias ($V > 0$) decreases it. A useful electrostatic length is the Debye length:

$$L_D = \sqrt{\frac{\varepsilon_s k_B T}{q^2 N}}, \tag{2.6}$$

with $N \simeq p_0$ in p-type or $N \simeq n_0$ in n-type material; L_D is the screening distance over which mobile charge neutralises potential perturbations and provides a quick consistency check for the depletion approximation near graded edges.

2.1.2 Carrier transport

Doping determines the majority-carrier type and the position of E_F at equilibrium, and, at the same time, defines the contact selectivity of conductivity. Introducing the mobilities μ_e and μ_h, the local conductivities are $\sigma_e = q\mu_e n$ and $\sigma_h = q\mu_h p$. At the electron-selective contact, one seeks $\sigma_e \gg \sigma_h$ so that electrons transmit while holes are blocked; at the hole-selective contact, one seeks $\sigma_h \gg \sigma_e$. Thin, wide-gap windows or transport layers, and ultrathin passivating/tunnelling inserts, strengthen this asymmetry without impeding majority extraction. Note that the difference in conductivities determines device operation, including architectures that rely primarily on carrier-selective layers.

In the classical *drift–diffusion* model, let ϕ denote the electrostatic potential and $\mathbf{E} = -\nabla\phi$ the electric field. The conduction-band edge satisfies $E_C(x) = -q\phi(x) + \text{const}$. In steady-state, isothermal, nondegenerate conditions, the carrier currents are

$$\mathbf{j}_e = q\mu_e n\mathbf{E} + qD_e\nabla n, \qquad \mathbf{j}_h = -q\mu_h p\mathbf{E} + qD_h\nabla p, \tag{2.7}$$

with D_e and D_h linked to the mobilities by Einstein's relation $D = \mu k_B T/q$.

Using Eq. (2.1), together with $\nabla E_C = q\mathbf{E}$ (from $E_C = -q\phi + \text{const}$) and Einstein's relation, taking $\nabla \ln n$ and $\nabla \ln p$ and substituting into the diffusion terms causes the field contributions to cancel exactly. The currents, therefore, reduce without further approximation to the quasi-Fermi-level form.

$$\mathbf{j}_e = \sigma_e \nabla E_{Fn}, \qquad \mathbf{j}_h = \sigma_h \nabla E_{Fp}, \tag{2.8}$$

which explicitly states that the gradients of the electrochemical potentials (the quasi-Fermi levels) are the macroscopic driving forces for transport.

Continuity couples transport to generation G and recombination R,

$$\frac{\partial n}{\partial t} = G - R - \nabla \cdot \mathbf{j}_e/q, \qquad \frac{\partial p}{\partial t} = G - R - \nabla \cdot \mathbf{j}_h/q,$$

and Poisson's equation (2.4) links ϕ to the space-charge density.

2.1.3 Under illumination

Open circuit. With open terminals, as shown in Figure 2.2a, the steady-state condition is $G = R$. Using Eq. (2.1), $np = n_i^2 \exp\!\left(\frac{E_{Fn}-E_{Fp}}{k_B T}\right)$. Inside the thin depletion region, the quasi-Fermi levels are nearly flat; the terminal photovoltage equals the splitting between the energy levels at the contacts:

$$qV_{OC} = E_{Fn} - E_{Fp}. \tag{2.9}$$

Introducing the dark recombination current density J_0, the short-circuit current density J_{SC}, and the ideality factor η, the illuminated current–voltage relation

$$J(V) = J_{SC} - J_0 \left[\exp\!\left(\frac{qV}{\eta k_B T}\right) - 1\right] \tag{2.10}$$

gives

$$V_{OC} = \frac{\eta k_B T}{q} \ln\!\left(\frac{J_{SC}}{J_0} + 1\right). \tag{2.11}$$

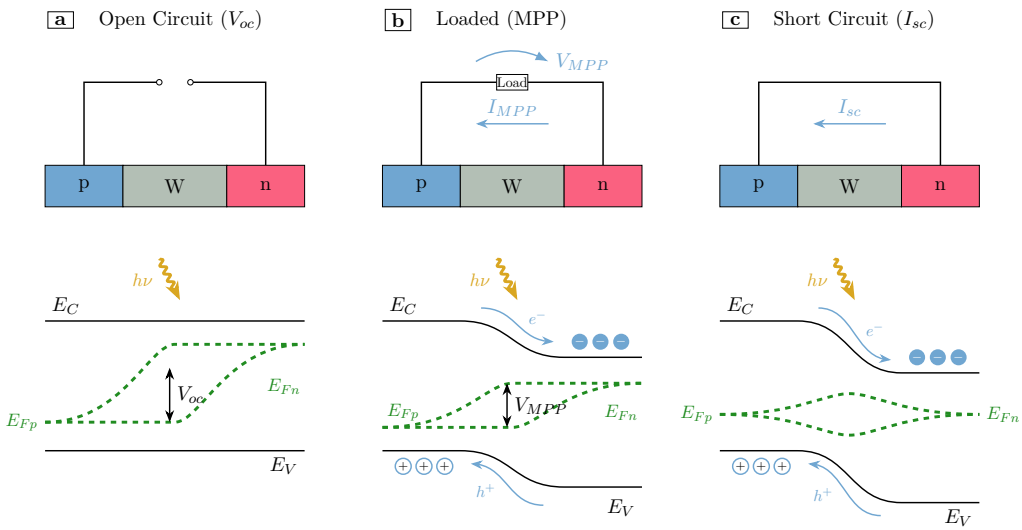

Figure 2.2: Band diagrams for a p–n junction under illumination. **(a) Open circuit (V_{OC}):** In the absence of external current extraction, the separation between the quasi-Fermi levels E_{Fn} and E_{Fp} is maximal, corresponding to the photovoltage at the terminals. **(b) Maximum power point (MPP):** Under a finite load, a voltage V_L is established, reducing the internal barrier compared to equilibrium and allowing power extraction. **(c) Short circuit (J_{SC}):** With $V = 0$, the quasi-Fermi levels converge toward the contacts, reflecting maximal collection of photogenerated carriers.

Short circuit. At $V = 0$, as shown in Figure 2.2c, the terminal current equals the net extracted photocarriers. Interband absorption for photon energy $h\nu \geq E_g$ sets the local generation profile.

$$G(x; \hbar\omega) = \alpha(\hbar\omega)\Phi(\hbar\omega)\ e^{-\alpha(\hbar\omega)x}, \tag{2.12}$$

where α is the absorption coefficient and Φ the spectral photon flux. Device optics, such as anti-reflective coatings, texturing, and light trapping, reshape $G(x)$. The local collection probability, set by fields, transport, and recombination, defines the internal quantum efficiency IQE(λ); spectrally, the short-circuit current density is

$$J_{SC} = q \int \mathrm{EQE}(\lambda)\Phi(\lambda)\ d\lambda \qquad \mathrm{EQE} = A \cdot \mathrm{IQE} \tag{2.13}$$

with A the absorptance and EQE the external quantum efficiency, defined as the ratio of the number of extracted charge carriers to the number of incident photons at a given wavelength.

Maximum power point (MPP). With a finite load, as shown in Figure 2.2b, the operating point is the intersection of the illuminated diode curve and the load line. The power density $P(V) = J(V)V$ peaks at the maximum power point, and the fill factor is

$$\mathrm{FF} = \frac{J_{\mathrm{MPP}}\, V_{\mathrm{MPP}}}{J_{SC}\, V_{OC}}. \tag{2.14}$$

Series resistance depresses V_{MPP}, as quasi-Fermi drops are needed to sustain current, while shunt paths reduce low-voltage current. High majority-carrier conductivity in transport regions and strong contact selectivity preserve V_{MPP} and FF.

2.1.4 The ideality factor η

The ideality factor η parameterises how the exponential part of the J–V curve responds to applied voltage:

$$J(V) \simeq J_0 \exp\!\Big(\tfrac{qV}{\eta k_B T}\Big) \quad \text{(forward bias, moderate } V\text{)}.$$

It measures the effective coupling between the terminal voltage and the internal quasi-Fermi separation that drives recombination. In the ideal diffusion/radiative case, $\eta = 1$; when depletion-region Shockley–Read–Hall recombination dominates, η tends toward 2. Intermediate values reflect mixed mechanisms or spatially distributed recombination, which can be ascribed to different origins:

- *Drift/diffusion in quasi-neutral regions:* Minority carriers injected across the junction recombine primarily in the quasi-neutral bulk with rates proportional to excess minority density; this is the ideal diode with $\eta = 1$.
- *Depletion-region SRH recombination:* If midgap defects are significant in the space-charge region, the recombination current there scales approximately with $\exp(qV/2k_BT)$, giving $\eta \simeq 2$ (low-level injection). [49]
- *High-injection and series resistance:* At high forward currents, injected carriers become comparable to majority densities (high injection), and ohmic drops appear in quasi-neutral regions; both effects can yield apparent $\eta > 1$ and curvature in semi-log J–V.

- *Heterojunction/transport layers:* Voltage can drop partly across transport layers or at interfaces; if recombination is localised in regions that do not experience the full terminal quasi-Fermi splitting, the extracted η exceeds 1.

Since recombination currents are proportional to integrals of np over regions where recombination occurs, and $np \propto \exp[(E_{Fn} - E_{Fp})/k_BT]$, η quantifies how efficiently the terminal voltage V maps onto the local quasi-Fermi separation *in the active recombination zone(s).* If the recombination sees only a fraction of the terminal splitting, e.g. barriers, band offsets, imperfect transport, the apparent η rises above 1.

2.1.5 Diffusion length of minority carriers

In low-level injection, minority-carrier transport in a quasi-neutral region obeys $D = d^2\Delta n/dx^2 - \Delta n/\tau = 0$ with solution $\Delta n(x) = Ae^{x/L} + Be^{-x/L}$ and

$$L = \sqrt{D\tau}, \qquad D = \frac{\mu k_B T}{q}, \tag{2.15}$$

where D and μ refer to the diffusion coefficient and mobility of the relevant minority carrier. The lifetime τ is the harmonic sum of radiative, SRH, Auger, and surface components. It sets the distance a minority carrier can diffuse before recombining, determines how much of the generated photocarriers can be extracted, and links process parameters such as surface passivation directly to J_{SC} and indirectly to V_{OC}, since a longer τ reduces J_0. These concepts are taken into account in the device and optical design.

In this framework, surface recombination plays an important role, as NWs have a high surface-to-volume ratio. At a surface $x = 0$, defect states can remove carriers at a rate quantified by the surface recombination velocity S. In 1D, the minority-carrier flux equals the net removal rate:

$$\mathbf{j}_e \cdot \hat{\mathbf{n}}\big|_{x=0} = qS_n\Delta n(0), \qquad \mathbf{j}_h \cdot \hat{\mathbf{n}}\big|_{x=0} = qS_p\Delta p(0) \tag{2.16}$$

An optimal surface passivation leads to small S and allows higher minority excess at the surface and hence higher collection; large S reduces Δn and Δp near the surface, reducing the collection of carriers generated close to the surface.

2.1.6 Esaki tunnel diodes

An Esaki (interband) tunnel junction (TJ), illustrated in Figure 2.3 is a heavily degenerate p^{++}–n^{++} junction. Its depletion region is sufficiently narrow to permit direct band-to-band tunnelling. Its J–V characteristic features a low-forward-bias tunnelling branch and a regime of negative differential resistance (NDR) as the occupied and empty states move out of resonance. At higher forward bias, there is a transition to the ordinary diffusion/excess current of a conventional p–n junction [50–52].

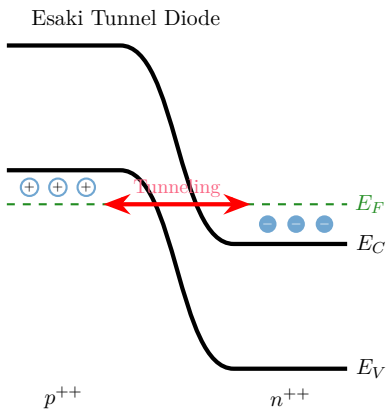

Figure 2.3: Energy band diagram of an Esaki diode featuring degenerate doping levels. The overlap between the conduction band on the n-side and the valence band on the p-side enables carrier tunneling (red arrow), the primary transport mechanism under reverse and low forward bias.

In a two-terminal tandem architecture, the tunnel junction (TJ) is deliberately operated very close to zero bias, on its quasi-ohmic low-forward-bias flank, so that it provides majority-carrier recombination between sub-cells with minimal series loss. Electrical and optical transparency are achieved by implementing very thin, wide-band-gap, heavily doped layers, and by controlling interfacial fields to avoid parasitic recombination [53].

Because the TJ is in series with the photovoltaic junctions, the tandem current equals the sub-cell current throughout the stack. The terminal voltage is the sum of all voltage drops, described by the equation:

$$V_{tot} = V_{op} - V_{TJ} + V_{bot}, \tag{2.17}$$

The minus sign reflects the Esaki diode's orientation relative to the photovoltaic

junctions. In operation, V_{TJ} remains small compared to the sub-cell voltages.

A central electrical constraint is that the tunnel diode's *peak tunnelling current density* J_{peak} exceeds the series J_{SC}). If $J_{\text{peak}} < J_{\text{SC}}$, the TJ limits current at low forward bias; with appreciable series resistances characterised by (*hysteresis*) since multiple operating points exist in the NDR region [54, 55].

Different regimes arise from the bias applied: under reverse bias the TJ is highly conductive, as electrons tunnel from the p^{++} valence band into empty conduction-band states on the n^{++} side; at low forward bias, alignment of occupied and empty states yields a large tunnelling current; as the forward bias is increased further and the energetic alignment between these states is lost, the tunnelling current decreases even though the voltage increases, resulting in negative differential resistance (NDR); at sufficiently high forward bias, tunnelling becomes negligible and the junction behaves as a conventional p–n diode dominated by diffusion and excess currents. Solar cells are operated at low bias conditions for the Esaki, which allow to avoid the problematic NDR region, keeping the TJ near the quasi-ohmic tunnelling [50–52].

From a materials and integration standpoint, wide-gap, very thin, heavily doped layers are preferred for the TJ to achieve a balance between electrical and optical transparency. Diffusion barriers and controlled thermal budgets help limit dopant spill-over, which would otherwise degrade sub-cell selectivity and V_{OC} [54].

2.2 Multi-junction solar cells

Multi-junction (MJ) solar cells stack semiconductor absorbers with *different* band gaps to harvest complementary spectral slices and reduce thermalisation and transmission losses. The stack can be contacted in several ways, leading to **two-terminal (2T)**, **three-terminal (3T)**, and **four-terminal (4T)** architectures. Each architecture trades off device simplicity, electrical constraints, optical coupling, and module-level interconnection complexity [56].

Two-terminal (2T) tandems. In 2T tandems, in Figure 2.4a, the subcells are series-connected and therefore must pass the same current; the device current is limited by the lowest-current subcell, while the open-circuit voltage adds approximately as the sum of the subcell voltages. This *current-matching* constraint tightens the allowable top/bottom band-gap pair and thickness window and can make the energy yield sensitive to spectral and temperature variations if not properly designed. Nonetheless, when current-matched and optically/electrically

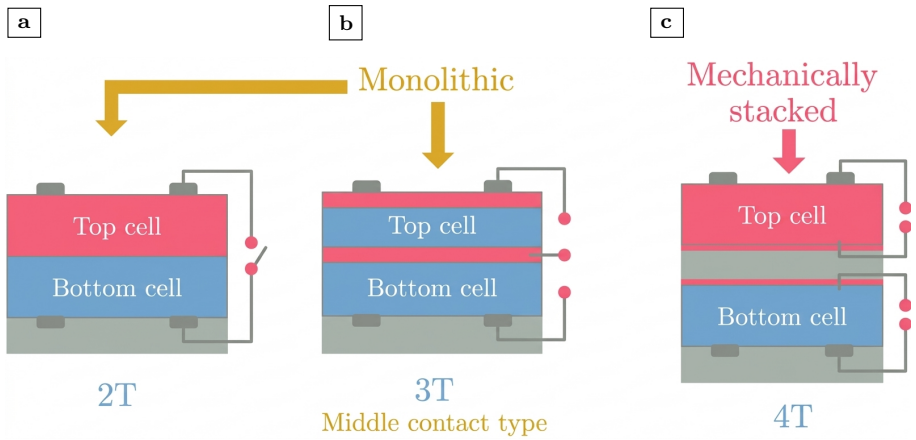

Figure 2.4: Tandem solar-cell architectures. (a) In 2T (monolithic) devices, subcells are series-connected and must operate at the same current. (b) 3T designs introduce a middle terminal that decouples subcell currents while maintaining mechanical integration. In 4T (mechanically stacked) tandems, each subcell operates at its own maximum-power point, though additional transparent interlayers introduce optical and electrical losses, and wiring complexity increases the overall system cost.

optimised, 2T tandems can match or exceed the annual energy production of 4T tandems once realistic interconnection losses are included [56].

Three-terminal (3T) tandems. Three-terminal tandems introduce an additional terminal, typically a *middle* or back contact (Figure 2.4b), that decouples the subcell currents while preserving mechanical integration. They thereby relax current-matching, expand the viable band-gap design space, and can deliver higher energy yield than 2T in variable outdoor conditions; however, they also introduce new measurement and loading conventions (two coupled outputs) and additional contact/series pathways that must be standardised for fair comparison. The community now uses a unified *taxonomy* for 3T devices (e.g., "series-type," "reverse-type," "split-terminal" designs) and recommends reporting conventions that sum subcell powers at their stabilised operating points under clearly specified loading topologies [57].

Following the 3T taxonomy and measurement guidance [57], the total device power is the algebraic sum of the simultaneously extracted subcell powers under the specified loading topology (e.g., one port held at a bias while the other is swept, or simultaneous MPP tracking in two dimensions); "zero-power points" play a role analogous to V_{OC} and J_{SC} for each subcell. Consistent reporting requires declaring: (i) the 3T category (e.g., series-type S, reverse-type R,

split-terminal, etc.), (ii) loading topology and stabilised operating condition, and (iii) any coupling (electrical/optical) modelled or measured (e.g., luminescent coupling)

From a *module* perspective, voltage-matched strings of 3T cells can avoid current-matching constraints while keeping interconnection complexity lower than fully independent 4T strings; rigorous analysis compares 2T, 3T, and 4T at the module level under real spectra, temperature, and wiring losses [56].

Four-terminal (4T) tandems. In 4T tandems (Figure 2.4c), each subcell has its own pair of terminals and operates at its independent maximum-power point; by construction, current matching is not required, and the optical/electrical design of each subcell can be optimised separately. In principle, this yields the highest cell-level power. In practice, the required transparent conducting interlayers and lateral current transport between subcells introduce *optical* (parasitic absorption, back-scattering) and *electrical* (sheet-resistance, grid shading) penalties that erode the advantage, especially in module form. Recent optics/TCO design studies and experimental 4T work quantify these penalties and show routes to mitigate them (e.g., optimised TCO thickness/mobility, finger pitch, and refractive-index matched interlayers), but they remain system-level considerations when comparing architectures [58].

3 | Methods

3.1 Metalorganic Vapour Phase Epitaxy

Metalorganic Vapour Phase Epitaxy (MOVPE) is a vapour–solid method in which volatile group–III and group–V precursors are transported to a heated crystalline substrate, where they adsorb, decompose, and incorporate epitaxially. The growth rate and film quality result from the balance of (i) hydrodynamics and diffusive transport across the near-substrate boundary layer, and (ii) surface reaction kinetics comprising adsorption, ligand elimination, surface diffusion, incorporation at steps, and desorption of by-products [59, 60].

3.1.1 Growth regimes and reactor design

At sufficiently low temperature or pressure, the growth rate is limited by surface reactions; at intermediate temperature, mass transport through the hydrodynamic boundary layer dominates; at high temperature and long residence times, parasitic depletion (wall reactions, gas-phase decomposition, homogeneous nucleation) can emerge. Reactor design (horizontal, vertical, radial/planetary) and operating pressure (atmospheric or reduced pressure) are chosen to minimise recirculation and dead volumes, thin the boundary layer where desired, and enable rapid, well-defined gas switching for abrupt heterointerfaces. The epitaxial growth of the nanowire arrays discussed in this thesis was performed using an Aixtron 200/4 horizontal flow reactor, which is schematically shown in Figure 3.1.

The input V/III ratio is a practical handle on the interfacial stoichiometry. Under conditions where group–III species are fully consumed at the growth

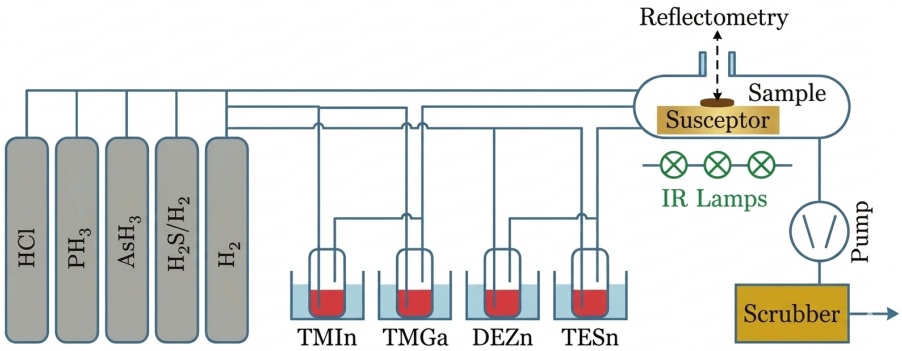

Figure 3.1: Simplified schematic of an Aixtron 200/4 MOVPE reactor showing hydrides supplied from high-pressure cylinders and metalorganic precursors from temperature-controlled bubblers, with separate delivery lines preventing intermixing before the growth chamber.

front, changing the group–V flow primarily adjusts the effective V/III at the interface, thereby influencing surface reconstructions, defect propensities, and the branching between competing surface reaction pathways.

3.1.2 Gas precursors

Group–III sources. Trimethyl and triethyl metalorganics remain the principal group–III precursors. Trimethylgallium (TMGa), trimethylaluminium (TMAl), and trimethylindium (TMIn) offer high vapour pressures and efficient surface-mediated decomposition over the relevant temperature range. TMIn is the most common In source due to its compatibility with atmospheric-pressure growth of InP and related alloys, and its high reaction efficiency. TMGa is commonly used for growing Ga-based semiconductors due to its significantly lower cost [36, 61–65]. Triethylgallium (TEGa) is widely used as an alternative to TMGa because it pyrolyses at significantly lower temperatures [66], making it a more efficient Ga source under the low-temperature conditions [66–68].

Group–V sources. Arsine (AsH_3) and phosphine (PH_3) remain standard group V sources. Their markedly different thermal cracking kinetics require higher V/III (and/or precracking or higher T) for PH_3 than for AsH_3. Organometallic group–V alternatives, notably tertiarybutylarsine (TBAs) and tertiarybutylphosphine (TBP), known for their low toxicity, enable lower pyrolysis temperatures and can provide uniform, device-quality layers across several III–V systems at

the expense of a complex decomposition chemistry and high manufacturing cost.

Dopant precursors. Intentional doping in MOVPE employs gaseous precursors that deliver the dopant to the growth front with controllable incorporation and minimal memory effects. In the context of this work, III-V nanowires and in particular *InP* and *GaAs*, for p-type layers, diethylzinc (DEZn) is used owing to its high solubility and shallow acceptor level, with ionisation energy $\sim$30 meV, though its relatively fast diffusion at typical growth temperatures constrains thermal budgets and junction abruptness. For n-type layers, hydrogen sulphide (H_2S) supplies sulphur on the group-V sublattice with efficient incorporation; however, despite the strong thiol bond [69], it does not alloy with the Au particle, reducing the memory effect while providing a high doping concentration. Sn can be introduced from tetraethyltin (TESn) and, in contrast to S, alloys with the Au particle; as a group-IV element, Sn is amphoteric in III–V compounds, though in III-V nanowires it is reported to act as a donor. In practice, choice of DEZn, H_2S, or TESn [64] is guided by the target conductivity type, required abruptness, and post-growth thermal constraints, while growth conditions are tuned to fix lattice-site selectivity and maximise the degree of electrical activation.

3.1.3 Bubblers and Epison

Metalorganics are commonly delivered from temperature-controlled bubblers, where carrier gas establishes an outlet partial pressure governed by the precursor's vapour pressure at the setpoint. Accurate delivery requires stable thermal control, well-characterised vapour curves, minimal pressure drops and cold spots, and short, purged switching manifolds to sharpen transients. In-line metrology, such as Epison-type acoustic/ultrasonic flow–concentration sensing, can track the actual precursor partial pressure and molar flow in real time. Coupled with pressure control and in-situ optical probes (e.g., reflectometry), this enables closed-loop control of composition, growth rate, and interface transients with production-level uniformity.

3.1.4 Operational principles

The MOVPE process relies on supplying metal–organic group-III precursors and group-V hydrides in the vapour phase, where thermal decomposition on a heated substrate leads to crystalline epitaxial growth. Once the precursor mixture enters the reactor, the carrier gas establishes a laminar flow profile over the susceptor.

The flow geometry, reactor pressure, and total gas velocity together determine the thickness of the diffusion boundary layer that separates the well-mixed gas stream from the near-surface region. In this regime, surface reaction kinetics are sufficiently fast that incorporation becomes mass-transport limited, with the flux of reactive species set by diffusion from the high-concentration gas phase toward the substrate, driven by the concentration (chemical potential) gradient.

As the precursor molecules approach the heated substrate, several reaction pathways may occur simultaneously, as shown in Figure 3.2. In favourable conditions, parent molecules reach the surface largely intact, where they physisorb or weakly chemisorb before undergoing heterogeneous pyrolysis. The released group-III and group-V species then form chemisorbed fragments that migrate across the surface until they are incorporated into energetically favourable lattice sites. Depending on the local temperature, pressure and precursor chemistry, part of the decomposition may instead occur upstream in the gas phase or lead to adduct formation, resulting in the subsequent removal of these products in the gas phase [59]. If the temperature or partial pressures are too high, however, undesired parasitic reactions dominate, consuming precursor flux and potentially generating particles or powder suspended in the gas stream. These parasitic channels modify the local stoichiometry. While a limited amount of material deposited on the reactor walls can establish a stable background partial pressure, excessive deposition, especially of strained material, can induce film cracking and lead to crystal debris falling onto the susceptor and substrate.

Once adsorbed and pyrolysed, the reactive surface fragments diffuse until they either desorb or incorporate into the crystal. The incorporation process depends critically on the density of steps, kinks and other low-energy sites available on the growth front. At low substrate temperatures, the pyrolysis and incorporation reactions are slow, and the growth rate follows Arrhenius behaviour, characteristic of the kinetically limited regime. Increasing the temperature eventually moves the system into the mass-transport-limited regime, where decomposition at the surface is rapid and the overall growth rate is determined by the rate at which precursors diffuse across the boundary layer. Further increases in temperature enhance desorption and promote precursor depletion via homogeneous reactions, ultimately reducing the net deposition rate.

Throughout the process, ligand fragments and other by-products formed at the surface must desorb efficiently and be swept away by the carrier gas. Stable exhaust conditions are essential to avoid re-adsorption of by-products, back-diffusion of contaminants, or virtual leaks that would perturb the precursor partial pressures. The interplay between hydrodynamic transport, gas-phase chemistry, and interfacial reaction kinetics therefore forms a tightly coupled system. The

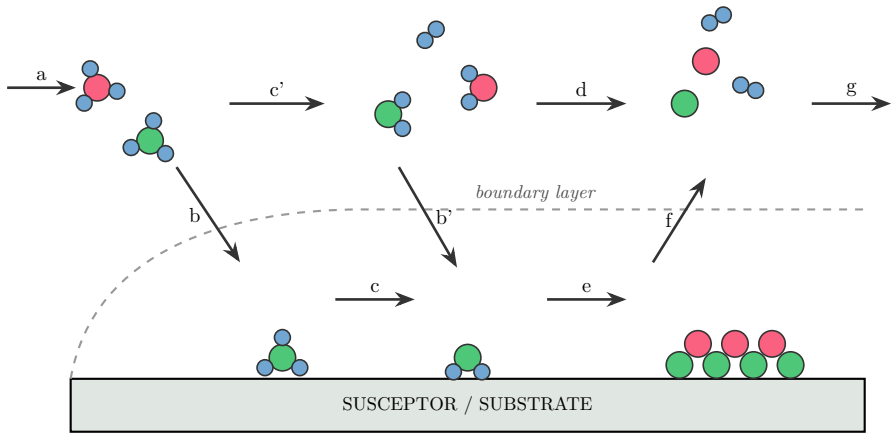

Figure 3.2: Schematic illustration of the elementary steps of MOVPE. (a) Precursor gases are transported into the reactor chamber. (b) Diffusion through the boundary layer and adsorption onto the heated substrate (b' intermediate species). (c) Heterogeneous pyrolysis of adsorbed precursors on the surface (c': homogeneous gas-phase pyrolysis). (d) Gas-phase reactions that may lead to particle or powder formation. (e) Adatoms diffusion and crystallisation (f) Desorption of by-products and unreacted species and (g) removal to the exhaust. Adapted from [60] and [59].

precursor arrival flux determines the surface reaction rate, while the thermal expansion of the incoming gas at the surface shapes the boundary-layer composition and feeds back on the mass transport upstream.

3.2 Talbot Displacement Lithography

Talbot Displacement Lithography (TDL) exploits the Talbot self-imaging of a periodic, phase-shift mask under deep-UV illumination. The diffracted orders form a three-dimensional intensity lattice that reproduces the mask pattern at axial intervals (Talbot periods). During exposure, the substrate is translated along the optical axis through multiple Talbot periods, thereby integrating the optical field, reducing sensitivity to the exact gap, and yielding uniform, wafer-scale periodic patterns without contact [70].

The methodology relies on the Talbot effect, where coherent light passing through a periodic pattern generates several diffraction orders that replicate the mask's pattern at regular axial intervals. The Talbot distance is

$$D_T = \frac{\lambda}{1 - \sqrt{1 - \lambda^2/p^2}} ,$$

with λ the illumination wavelength and p the pitch of the periodic mask [71].

For catalyst patterning, a double-resist stack is used in which a developable bottom layer acts as a non-imageable anti-reflective coating and simultaneously provides the undercut needed for lift-off. A common stack consists of a deep-UV resist on PMGI: after exposure and development, the PMGI undercut is already formed, and the diameter of the resist openings can be tuned by the accumulated dose. This enables two routes with a single mask: (i) direct transfer of 200 nm holes into a dielectric by reactive-ion etching to obtain an epitaxial growth mask, or (ii) metal deposition and lift-off to obtain Au nanodiscs for vapour-liquid-solid (VLS) nanowire seeding, as illustrated in Figure 3.3. DTL in III–V systems has been benchmarked in several works demonstrating sub-100-nm periodic arrays with excellent wafer-scale uniformity and high resolution; however, achieving these results requires precise control over both stage motion and environmental humidity [70, 72, 73]. The catalyst arrays then define the seed diameter and pitch for subsequent MOVPE nanowire growth in the VLS configuration, preserving the pattern fidelity inherited from the DTL mask [70].

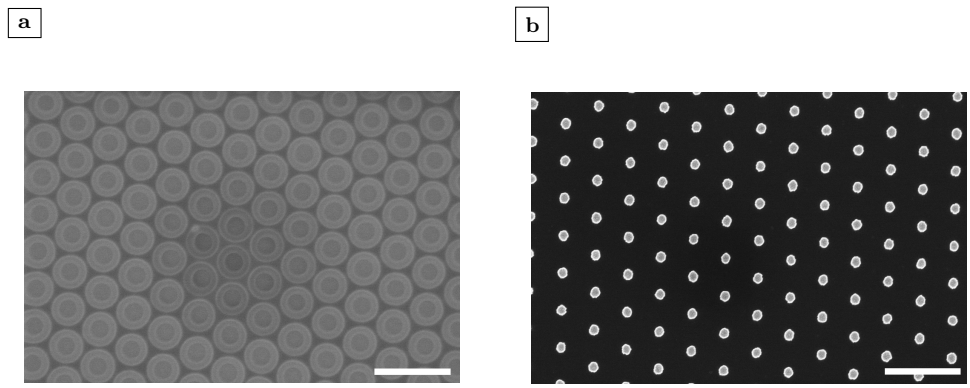

Figure 3.3: SEM images of results of Displacement Talbot Lithography exposure. (a) Exposed double-resist stack; the inner circles set the Au seed diameter. Scale bar: 1 μm. (b) Au seed particles after lift-off. Scale bar: 1 μm.

3.3 Catalyst-assisted axial growth

The vapour–liquid–solid (VLS) mechanism, originally formulated for Au–Si whiskers [74, 75], provides the foundational description of Au-assisted nanowire growth, and its concepts apply as well to III-V semiconductors. Under typical MOVPE conditions, the catalyst particle may be liquid, partially solidified, or entirely solid depending on its composition and the growth temperature [76, 77].

As precursors are supplied, group-III species dissolve into the Au particle, leading to the formation of a liquid eutectic droplet (Fig. 3.4b). Regardless of its phase state, axial growth is governed by the *supersaturation at the particle–nanowire interface*. Once the concentration exceeds the solubility limit, precipitation occurs underneath the Au catalyst particle, initiating the nucleation of the semiconductor bilayer (Fig. 3.4c).

In the steady-state regime (Fig. 3.4d), the interface conditions result from three coupled factors: (i) the *effective* V/III ratio at the droplet–facet interface, set by precursor arrival and desorption; (ii) the *adatom flux* collected on the substrate and nanowire sidewalls and subsequently transported into the particle [78–80]; and (iii) the *instantaneous droplet state*: its composition, and wetting angle [81, 82]. These parameters evolve continuously during growth, giving rise to dynamic shifts in supersaturation and nucleation behaviour.

The axial growth cycle proceeds through four coupled steps as illustrated in Figure 3.4. First, group-III species dissolve into the catalyst until the chemical potential exceeds the solubility limit [75]. While group-V species impinge on the particle and the triple-phase line (TPL), owing to their negligible solubility in Au, they participate directly in nucleation at the interface. Heterogeneous nucleation initiates at the TPL, where the interfacial energy budget is minimised [83, 84], local fluctuations in droplet shape and wetting angle may further lower the nucleation barrier [82]. Finally, the new bilayer spreads laterally across the top facet until completion [82, 85, 86].

Both the supersaturation threshold and the nucleation pathway are strongly influenced by the local V/III ratio and the diffusive flux of group-III adatoms from the surrounding surfaces [79, 80, 87]. The axial growth rate is determined by the combined contributions of direct impingement on the droplet and adatom-mediated supply, while the nucleation attempt frequency is dictated by the droplet supersaturation; the droplet's evolving contact angle modulates the size of the nucleation perimeter and the preferred crystal phase [82, 84].

Crucially, while the catalyst promotes axial elongation, the group-III adatom flux may also contribute to vapour solid growth on the substrate surface. This results in parasitic growth that competes with the nanowire for precursor consumption, potentially affecting the final homogeneity and composition of the ternary compound [88, 89].

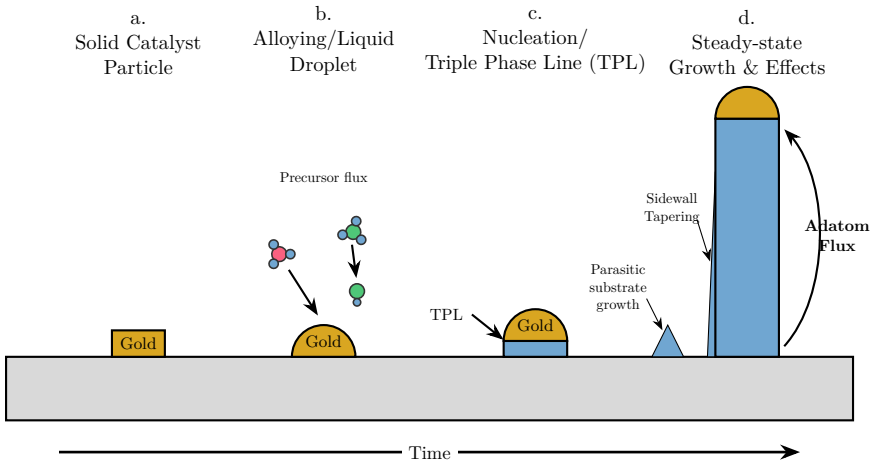

Figure 3.4: Schematic representation of the VLS growth mechanism. (a) Solid Au catalyst particle on the substrate. (b) Alloying stage: group-III precursors saturate the Au seed, forming a liquid eutectic droplet. (c) Nucleation: reaching supersaturation leads to the precipitation of the first semiconductor bilayer at the interface. (d) Steady-state axial growth, highlighting the adatom flux and the competition with external substrate and sidewall parasitic growth. Adapted from [74].

3.3.1 Gallium Arsenide

Gallium arsenide (GaAs) has played a central role in establishing the foundations of III–V nanowire research. As a direct–bandgap semiconductor with high carrier mobility, GaAs rapidly proved attractive for nanoscale optoelectronics. In nanowire geometry, it further distinguishes itself by combining reliable catalyst–assisted growth, strong tunability of crystal phase, and consistently high structural and optical quality under appropriate conditions. Historically and conceptually, GaAs therefore became the reference material for understanding III–V nanowire growth dynamics.

The earliest demonstrations of III–V nanowires grown by MOVPE showed that trace surface Au on GaAs(111)B initiates vapor–liquid–solid (VLS) nanowhisker growth with diameters down to 20–30 nm [90, 91]. These studies established that Ga accumulates in the Au particle after precursor decomposition and that axial growth initiates once the droplet becomes supersaturated and nucleates a new monolayer at the liquid–solid interface. Even in these first experiments, GaAs nanowires exhibited wurtzite (WZ) segments, rotational twins, and stacking faults, highlighting the material's inherently flexible stacking sequence under $\langle 111 \rangle$B growth. Such polytypism would later become central to both fundamental studies and device concepts.

GaAs nanowires are typically grown by MOVPE between 400–550 °C. In this range, the Au–Ga droplet remains supersaturated in Ga while maintaining a stable wetting configuration at the triple–phase line, enabling rapid layer–by–layer nucleation. At temperatures above this window, parasitic deposition on the sidewalls increases markedly, resulting in tapering and loss of diameter control. At lower temperatures, the decomposition of TMGa becomes rate–limiting, as supported by classical MOVPE pyrolysis studies [92]. Under such conditions, axial growth persists but with significantly reduced precursor supply, making droplet supersaturation and Ga transport the limiting steps [78, 93].

The state of the Au catalyst and its wetting configuration at the triple–phase line have also been shown to influence nucleation behaviour, defect formation, and growth direction [79, 85, 94]. RHEED and TEM studies demonstrate that small changes in droplet composition or contact angle can alter the nucleation barrier for zincblende (ZB) versus wurtzite (WZ) stacking and can thereby promote stacking faults, rotational twins, or extended WZ segments [77, 95]. Such sensitivity arises because the crystal phase is selected during the monolayer nucleation at the droplet perimeter, where the balance of interface energies and supersaturation determines whether a ZB or WZ nucleus is thermodynamically favoured.

This polytype tunability directly influences the optical properties of GaAs nanowires. Defects such as rotational twins or stacking faults introduce type–II band offsets at ZB/WZ interfaces, which localise carriers and modify recombination pathways [96]. Pure WZ segments exhibit a slightly larger bandgap than ZB GaAs, while mixed–phase regions can host quantum–disk–like states with characteristic redshifted emission. These features are relevant for optoelectronic applications, since both radiative efficiency and carrier transport depend sensitively on the local stacking sequence. For high–quality GaAs nanowires free of planar defects, photoluminescence spectra are dominated by near–band–edge emission, reflecting the material's intrinsically favourable optical characteristics.

3.3.2 Indium Phosphide

Indium phosphide (InP) emerged among the III–V semiconductors, particularly for high-speed electronics and photonic devices operating at telecommunication wavelengths. InP nanowires combine excellent intrinsic optical properties and a low surface recombination velocity compared to other III-V semiconductor materials [97, 98]. The introduction of the HCl enabled a larger parameter space for InP growth, which became a key model system for understanding precursor chemistry, droplet-mediated supersaturation, and the origins of polytype

formation in III–V nanowires [99–104].

Early MOVPE experiments demonstrated that vertically oriented, uniform InP nanowires can be grown using Au seed particles under low-pressure conditions [105]. In these studies, trimethylindium (TMI) and tertiary-butyl phosphine (TBP) act as precursors, and the Au particle forms a nanoscale Au–In eutectic droplet after a high-temperature annealing step. This droplet establishes the vapor–liquid–solid (VLS) growth front and acts as an efficient sink for group-III species. Growth occurs at temperatures around 430–500 °C, yielding nanowires with diameters of 20–25 nm and lengths around 700 nm after only one minute of growth. These early InP nanowires already exhibited rotational twins and stacking faults along the $\langle \bar{1}\bar{1}\bar{1} \rangle$ axis of the NW, features typical of III–V nanowire growth where monolayer nucleation at the triple-phase line sensitively determines the local stacking sequence [105].

Growth-parameter dependencies indicate that InP nanowire formation is governed by the balance between droplet supersaturation and the kinetic suppression of substrate growth. At low temperatures, incomplete TMIn decomposition limits the material supply to the Au-In droplet, preventing sustained supersaturation and resulting in negligible axial growth. At intermediate temperatures, efficient precursor cracking enables droplet supersaturation, leading to nucleation and precipitation, while substrate growth remains kinetically limited, favouring stable axial nanowire growth. At higher temperatures, enhanced adatom mobility and efficient crystal growth on the substrate reduce this kinetic selectivity, suppressing nanowire formation despite adequate precursor decomposition [105]. This overall picture is consistent with more general kinetic analyses of III–V nanowire growth, which show that the balance between direct impingement, adatom diffusion, and droplet incorporation determines both axial and radial dimensions [78, 93]. Unlike GaAs, however, InP is particularly sensitive to the group-V precursor kinetics; an insufficient supply of P enhances the probability of defect formation and changes in droplet composition.

A distinctive feature of InP nanowires compared to their bulk counterpart is their polytypism. Undoped MOVPE-grown InP nanowires typically crystallise in the WZ structure, often containing numerous stacking faults [79, 106, 107]. The preference for WZ has been attributed to favourable surface energies of WZ side facets and nucleation energetics at the liquid–solid interface under VLS conditions. Algra *et al.* demonstrated that adjusting the droplet composition—particularly through Zn doping—can reversibly switch the crystal structure from WZ to ZB and even induce long-range ordered twinning superlattices (TSLs) [107]. Their work provides a quantitative model linking droplet shape distortion, nucleus geometry, and the free-energy governing monolayer nucleation. The ability to

control ZB/WZ phase selection and twin periodicity in InP nanowires represents one of the most advanced examples of phase-engineered III–V nanowires [108].

Optical characterisation shows the important material properties. MOVPE-grown InP NWs exhibit strong room-temperature and low-temperature photoluminescence (PL), frequently with a measurable blueshift relative to bulk InP due to quantum confinement in diameters of 20–30 nm [105]. At 77 K, additional shifts arise from strain relaxation effects specific to nanowire geometry, where lateral strain remains partially frozen, modifying the band structure. In addition, the inherently low surface recombination velocity of InP [98] allows efficient radiative recombination even in nanowires without dielectric passivation—an important advantage for optoelectronic applications such as single-nanowire photodetectors and light-emitting diodes. The strong excitonic emission observed in high-quality WZ and mixed-phase structures reflects the low density of nonradiative centres and the robustness of the electronic structure to variations in stacking sequence.

3.3.3 Gallium Indium Phosphide

Gallium indium phosphide ($Ga_xIn_{1-x}P$) is a composition-tunable ternary III-V compound semiconductor, with possible direct bandgap in the range 1.34–1.97 eV corresponding to composition $0 \leq x \leq 0.68$ [109]. It has long been the material of choice for the upper cell in record-efficiency III–V multijunction devices, since it is lattice-matched to GaAs for $x = 0.5$, but its thin-film growth remains challenging [12, 110–112].

In nanowire geometry, GaInP further benefits from the inherent elastic strain relaxation, enabling compositionally flexible hetero-interfaces that are difficult to realise in planar layers, allowing even WZ GaP with a direct bandgap of 2.1 eV [113]. These characteristics have made GaInP a key material for the top junction of axial III-V nanowire tandem solar cells and, more recently, as an efficient low-bandgap branch material in diffusion-driven light-emitting architectures [114, 115].

MOVPE growth of GaInP nanowires proceeds by the Au-assisted VLS mechanism, as detailed in section 3.3. However, GaInP exhibits a distinct sensitivity to precursor kinetics, particularly in the choice of group-III metalorganics. The gallium precursor was supplied by TEGa, since it provides a higher effective Ga supply, improved axial growth rate, and alloy homogeneity [66]; while indium was supplied by TMIn, which decomposes efficiently across the entire growth range. These kinetic differences make the input molar fractions and consequently the relative incorporation of Ga and In at the TPL the primary control parameters

for setting the alloy composition x in $Ga_xIn_{1-x}P$.

The optimal temperature range for GaInP nanowire growth is typically 420–480 °C. Within this window, precursor pyrolysis is sufficiently efficient to sustain supersaturation in the Au catalyst, while radial growth from vapour-solid pathways remains kinetically limited. At higher temperatures, enhanced gas-phase pyrolysis and increased adatom mobility promote significant radial deposition, tapering, and compositional gradients. These effects are amplified in ternary alloys: the unequal diffusion lengths and surface residence times of Ga and In adatoms strongly affect their incorporation probabilities, with Ga exhibiting a shorter surface diffusion length and higher desorption rate than In. As a result, inadvertent enrichment toward the tip or along the wire can occur unless the V/III ratio, pitch, and Ga precursor chemistry are optimised [64, 89].

Compositionally, GaInP nanowires pose challenges similar to those encountered in other ternary III-V systems. In adatoms may diffuse from the substrate or sidewalls into the catalyst droplet, especially at lower V/III ratios, causing an unintended axial increase in In concentration. Conversely, insufficient Ga pyrolysis can cause local Ga-limited growth, creating radial or axial composition gradients [116–118].

3.3.4 Control of the V/III ratio at the growth interface

The *effective* V/III at the particle–facet perimeter determines supersaturation, nucleation barrier, and polytype selection [119]. For Au-seeded GaAs, *As-rich* conditions bias ZB, while *Ga-rich* conditions bias WZ, consistent with in-situ and post-growth correlations between crystal phase and droplet wetting angle/-composition [79, 87, 120]. Importantly, the same nominal V/III change can traverse two *distinct regimes*: a group V-limited window at lower V/III and a group III-limited window at higher V/III. WZ appears when the effective arrivals of III and V at the interface are closely balanced; moving away from this balance produces first mixed stacking (short WZ/ZB segments) and then phase-pure ZB—either for low V/III (V-limited) or for high V/III (III-limited)[120]. Practically, the interface V/III is set by precursor flows and cracking, surface sticking and adatom lifetimes, the competition between axial and radial consumption, and the droplet state (composition and contact angle) [121].

In-situ TEM reveals complementary growth dynamics: zincblende segments often advance through a rapidly oscillating triple-phase line, whereas wurtzite segments grow predominantly by step-flow; transitions between the two correlate with changes in droplet wetting angle and alloy composition [79, 82, 87].

Additives and local tuning Gas-phase chlorides provide a direct means to tune the local III/V ratio and sidewall kinetics. In GaAs, introducing a controlled HCl flow during MOVPE does not significantly affect the Ga-containing species prior to incorporation; instead, it increases the interfacial V/III ratio and drives a transition from WZ (Ga-rich) to defect-free ZB, producing atomically abrupt WZ→ZB interfaces. The axial growth rate decreases accordingly, while well-defined {110} ZB facets. emerge [121].

In InP, HCl reacts predominantly in the gas phase, and likely also heterogeneously at the exposed surfaces, to form volatile $InCl_x$ species. Because the In-Cl bond is strong (∼1.5 eV) [122], these chlorinated indium species possess a much longer diffusion length than native In adatoms, resulting in strongly anisotropic, gas-phase–mediated etching. This mechanism suppresses tapering and enables decoupled control over axial and radial nanowire. evolution [99, 100].

3.3.5 In-situ LayTec reflectometry for real-time metrology

Multiwavelength optical reflectometry, such as LayTec EpiR/EpiTT, provides *in-situ* tracking of NW length, array-modal signatures, and instantaneous axial rate with sub-second resolution [123, 124]. Interference fringes formed by reflections at the array top and the substrate yield the length at wavelength λ via

$$L(t) \;=\; \frac{m(\lambda, t)\,\lambda}{2\,n_{eff}(\lambda)}\,, \tag{3.1}$$

where m is the fringe order and n_{eff} the pattern-specific effective index (set by pitch and diameter). In practice, $n_{eff}(\lambda)$ is pre-calibrated for each pattern or obtained from an initial fit, after which fringe counting provides real-time length and growth-rate traces. Short-time features-slope changes, phase shifts-mark gas switching and dopant on/off transients (e.g., DEZn), enabling immediate adjustment of flows and temperature to stabilise the targeted regime [123, 124].

3.4 Characterization methods

3.4.1 Scanning electron microscopy (SEM)

SEM forms images by scanning a tightly focused electron probe over the surface and detecting low-energy secondary electrons (SE) emitted from the near-surface region. Because the SE yield is influenced by edges and sidewall orientation, SEM

is particularly effective for tracking NW morphology. In this work, plan-view images at normal incidence are used to read out pitch, ordering, and site occupancy, whereas a modest stage tilt (30°) enhances sidewall contrast to extract axial length and taper; lengths from tilted views are corrected for the applied tilt. Low beam energies are chosen for dielectric or polymer-embedded arrays to keep the interaction volume shallow and to suppress charging; under these conditions, SE contrast remains dominated by topography rather than composition. Backscattered-electron detection is only invoked when qualitative Z-contrast is needed (e.g., to confirm a metal cap or contact layer), while SE images serve as the basis for quantitative metrology. The same field areas are revisited before and after processing steps (planarization, tip exposure, transparent contact deposition) to monitor changes in geometry and verticality, providing a consistent, non-invasive, purely geometrical characterisation used throughout to corroborate optical/EBIC measurements and to parameterise growth and processing models. Modern SEM often provide transmission mode electron microscopy (STEM). A converged probe is rastered through a thin lamella, and the transmitted electrons are recorded by annular detectors. Bright/dark-field STEM resolves defects and interfaces via diffraction contrast. STEM is used selectively for cross-checks when SEM metrology and electrical/optical data disagree or when sub-20 nm features must be resolved.

3.4.2 Electron-beam-induced current (EBIC)

EBIC probes the local carrier-collection efficiency by scanning a focused electron beam and recording the induced current between selective contacts. In the notation used throughout this thesis, the measured current at beam position a is written as

$$I_{EBIC}(a) \;=\; q\int_{x_{fc}}^{x_{bc}} g(x-a)\,\phi(x)\,dx,$$

where $g(x-a)$ is the generation profile (set by E_b and the stack) and $\phi(x)$ is the collection probability governed by drift in the space-charge region and minority-carrier diffusion in quasi-neutral regions [125, 126]. In low-injection conditions, $\phi(x)$ decays with an *effective diffusion length* L_{eff} that depends on bulk lifetime and surface recombination; via reciprocity, $\phi(x)$ equals the normalised minority-carrier distribution in the dark [125, 126]. Cross-section EBIC therefore enables extraction of x_{SCR} and L_{eff} (from E_b-dependent profiles), while plan-view EBIC maps lateral non-uniformities across arrays [125]. Practical pitfalls—surface recombination at the cross-section, high-injection artefacts, electron-channelling contrast, and unintended surface-current paths—are mitigated by moderate I_b, $E_b \gtrsim$ 8–10 kV, and amplifier ranges matched to nanoampere-scale signals [125,

126].

Single-NW devices in SEM For vertically standing single NW solar cells, a nanoprobe forms the top contact while the substrate/back electrode closes the circuit, whose schematic is illustrated in Figure 3.5. Coupling EBIC with an in-SEM, fibre-delivered LED allows light $I-V$ on the same NW and a direct comparison to its EBIC profile [127]. EBIC linescans reveal how junction depth, compensation in mid-segments, and surface recombination shape axial collection; the short-circuit current under optical excitation scales with the integrated collection near the optical generation maximum but does not track the EBIC area linearly because EBIC excitation volumes and injection levels differ from the optical case [127]. As an additional single-NW case study, EBIC can resolve oxide-induced field effects: embedding InP p–i–n NWs in PO_x/Al_2O_3, gives raise to surface fixed charges, which act as a parasitic junction, reducing the intensity of the electrostatic potential along the NW solar cell, which is visible as a systematic shift/reshaping of the EBIC peak [128].

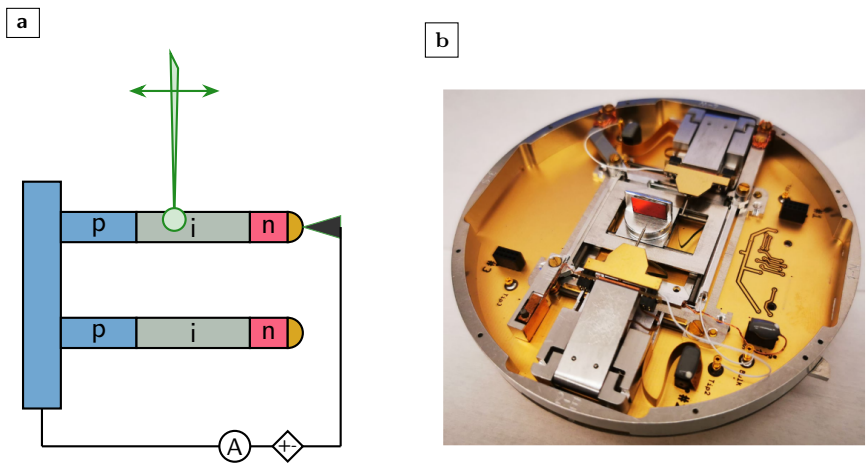

Figure 3.5: (a) Schematic of the single NWs EBIC measurements setup. (b) Image of the nanoprobe shuttle.

Processed NW arrays On fully processed arrays, plan-view EBIC rapidly discriminates contacted from non-contacted regions, identifies shunted patches, and quantifies the electrical impact of etch-back and top-contact geometry (e.g., dome- vs doughnut-like TCO around tips) [129]. Cross-section EBIC verifies that the as-grown axial collection is preserved after processing and separates contributions from the NW, embedding dielectric, and substrate; sweeping E_b

deconvolves ring-like perimeter signatures from the beam interaction volume [129]. For axially stacked sub-cells (e.g., GaInP/InP tandems), EBIC with controlled optical/electrical bias allows sub-cell-resolved mapping and the identification of parasitic junctions (e.g., at tunnel diodes) [130].

3.4.3 Current–voltage (I–V) and EQE

Illuminated $I-V$ curves are measured under $1000\,\mathrm{W\,m^{-2}}$ AM1.5G using a calibrated reference and spectral matching. The figures of merit–J_{SC}, V_{OC}, FF, η–follow the standard definitions; two-terminal tandems are verified by *voltage addition* and *current limitation* by the weaker subcell. For NW arrays, series resistance (front TCO/metal grid) and tip-contact resistance frequently limit FF; we combine dark and light $I-V$ with Suns–V_{OC} when needed to separate transport from recombination.

EQE(λ) is recorded with a monochromated, chopped probe and calibrated photodiode; DC bias light and electrical bias selectively activate subcells in tandem structures. We use

$$EQE(\lambda) \;=\; \frac{I_{ph}(\lambda)}{q\,\Phi(\lambda)}\,,$$

and the reciprocity between EQE and electroluminescence to cross-check junction quality and quasi-Fermi-level splitting in the radiative limit. In NW tandems, partial EQE with spectral biasing or reverse bias isolates the current-limiting subcell and quantifies parasitic absorption in transparent contacts and dielectrics.

3.5 Lithography

Photolithography is a parallel patterning technique that employs a physical photomask—typically a quartz plate with a patterned chrome layer—to shadow and transmit UV light onto a photoresist-coated substrate [131]. While this method allows for high-throughput manufacturing, it remains inherently rigid; any modification to the device architecture necessitates the fabrication of a new, costly mask set.
Mask-less lithography (MLA) removes the photomask from the exposure loop and writes patterns directly from a digital layout onto photoresist. Among mask-less approaches, a widely used class is *projected, spatial-light-modulator* (SLM) lithography, where a digital micromirror device (DMD) serves as a *virtual* mask. By utilising a DMD to modulate UV light at wavelengths of 375 nm or

405 nm, the system achieves spatial light modulation, enabling the direct-write of CAD-defined geometries with sub-micron resolution [132]. This digital approach is particularly advantageous for the fabrication of optoelectronic devices, as it enables real-time compensation for substrate bow and provides the flexibility to adjust contact geometries without the temporal or financial constraints of physical mask fabrication [133]. Furthermore, the non-contact nature of the MLA 150 minimises surface contamination, ensuring that the electronic and optical properties of the MOVPE-grown layers remain uncompromised during subsequent processing steps such as metallization or dry etching [134].

3.5.1 Atomic layer deposition

Atomic layer deposition (ALD) is a subtype of chemical vapour deposition in which the sample is exposed to precursor vapours in a cyclic manner. Each cycle ideally produces one atomic layer, allowing precise control over the total film thickness. Because the reactions are self-limiting and based on surface chemisorption, ALD provides conformal coatings even on high-aspect-ratio structures such as nanowires.

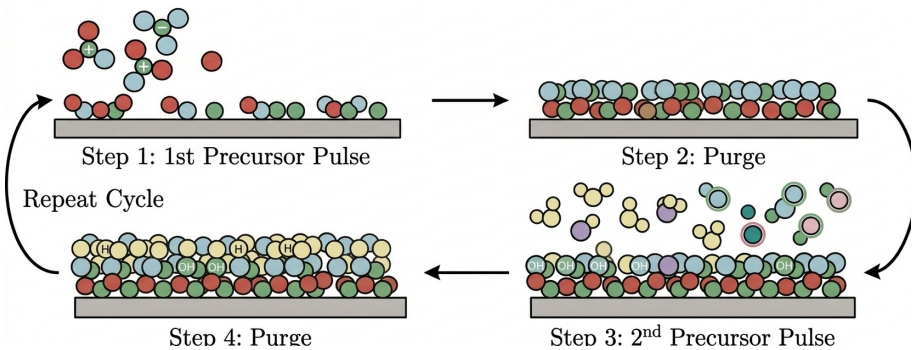

Figure 3.6: Schematic ALD cycle.

A typical cycle consists of several steps and uses two precursors in alternating sequence. First, the initial precursor chemisorbs onto available surface sites and forms a saturated monolayer. After a purge step removes excess precursor and by-products, a second precursor is introduced to react with the surface layer and form the desired material. A final purge completes the cycle, which can then be repeated until the target thickness is reached.

In this work, SiO_x and Al_2O_3 deposited by thermal ALD were used as the dielectric material. This process ensures the formation of dense, uniform films

at low temperature and demonstrates excellent conformity along the nanowire sidewalls.

3.5.2 Mixed Metal Halide Perovskites

Mixed metal–halide perovskites ($MAPb(I_{1-x}Br_x)_3$) have become a reference thin-film absorber by combining direct bandgaps and large absorption coefficients, together with a "soft" ionic lattice that confers high defect tolerance compared with more covalent semiconductors. Their bandgap can be tuned across the visible to meet the 1.7–2.0 eV window required for top or mid absorbers in multijunction solar architectures [22, 135, 136].

Broad analyses of perovskite devices show that process techniques proven efficient for bandgaps near 1.6 eV do not translate to wider bandgaps. In particular, a pronounced efficiency dip and a scarcity of stable, high-performance results emerge between 1.7–2.0 eV. Device-level studies attribute this behaviour to increased non-radiative losses (bulk and interfacial) and light-induced halide segregation in Br-rich alloys, yielding large V_{OC} deficits unless contact stacks and surfaces are re-optimised (e.g., via self-assembled monolayers, 2D/3D caps, and better-aligned charge transport layers) [137, 138].

Experimentally, the hallmark of segregation is an immediate red-shift and re-weighting of the PL spectrum under above-bandgap illumination, with emission funnelled into emergent iodide-rich (narrower-gap) domains even when these occupy a tiny volume fraction. Optical mapping and time-resolved probes reveal a multi-stage pathway. **Stage 1** (seconds): nanoscopic I-rich clusters nucleate and dominate the PL while the host remains largely unchanged optoelectronically apart from carrier funneling. **Stage 2** (minutes to hours): composition redistributes more broadly; the low-energy PL band stabilises as I-rich islands coarsen. Spatial PL maps indicate preferential nucleation where the initial PL yield is low, implicating defects and local chemistry [136, 139, 140].

These observations stringently test mechanism proposals. Representative thermodynamic pictures (polaron-induced strain or carrier free-energy/gap arguments) rationalise local stabilisation of low-gap pockets under carrier population [141, 142], but quantitative comparison shows that, at one-sun densities, the free-energy gain is insufficient to drive the large, film-wide composition shifts of Stage 2 [140]. A kinetic description is therefore required: illumination increases mobile point-defect densities (notably halide vacancies), raising the effective diffusivity in carrier-rich regions and enabling gradient-driven coarsening. Temperature-dependent optical tracking yields an activation energy of

$\sim$23 kJ mol^{-1} for the extended reorganisation (Stage 2), whereas Stage 1 remains temperature-independent, consistent with ultrafast funneling into nanoscopic I-rich clusters; a minimal 2D model coupling photo-activated, vacancy-assisted diffusivity to chemical-potential-driven transport reproduces the two-stage kinetics and their composition trends [140, 143].

Device-level consequences follow: in-situ tracking shows modest V_{OC} loss (tens to $\sim$100 mV) but a much larger J_{SC} drop, because carriers funnel into isolated I-rich pockets that are poor extraction pathways [144, 145]. Mitigation routes emphasised for wide-gap cells include (i) reducing interfacial recombination with tailored HTL/ETL energetics, SAMs, and ultrathin 2D caps; (ii) bulk and grain boundaries passivation (e.g., appropriate ammonium halides/alkanediammoniums); and (iii) composition/strain management to curb defect formation and slow ion migration, all of which improve PLQY, QFLS, and stabilised V_{OC} [138]. Finally, an observer effect is evident: at X-ray doses well below those that form PbI_2, XEOL quenching and transient low-energy emission appear, and controlled pre-doses can even suppress subsequent light-segregation, which is a direct evidence that defect chemistry governs both instability and its apparent mitigation [146].

3.6 Optical modelling

Geometrical optics provides a comprehensive framework for understanding how light interacts with macroscopic objects. In this formulation, light behaves as rays with defined paths of propagation, and its material properties are determined by its refractive index. The propagation of light through a medium adheres to Fermat's principle, asserting that light traverses the path that minimises travel time. The speed of light in a medium depends on its refractive index and is defined as $c = c_0/n$, where c_0 represents the speed of light in a vacuum.
At the interface between two media with distinct refractive indices, denoted as n_1 and n_2, an incident ray splits into two components: a refracted (transmitted) ray and a reflected ray, both lying within the incident plane. The relationship between the incident angle and the refraction angle follows Snell's law:

$$n_1 \sin\theta_1 = n_2 \sin\theta_2 \tag{3.2}$$

However, geometrical optics cannot describe effects arising from light's wave character and polarisation. In nanostructures, the object size is comparable to the wavelength of light. The interference of light waves scattered from these features

can dominate the optical response of the whole sample. Thus, appropriately modelling the optical response of nanostructures requires solving Maxwell's equations. Electromagnetic optics provides a description for phenomena such as interference, diffraction and polarisation. It comes from the intuition that light is an electromagnetic wave, with its polarisation characterised by the wave's vector.

In this work, Maxwell's equations are solved in JCMwave, which describes the electromagnetic field in the frequency domain [147]. The electromagnetic field is the sum of the harmonic components of angular frequency ω, thus can be described by the complex phasors $\boldsymbol{E}(r)$, $\boldsymbol{H}(r)$ of electric and magnetic field components respectively:

$$\boldsymbol{E}(\mathbf{r},t) = Re\{\boldsymbol{E}(\boldsymbol{r})e^{-i\omega t}\} \tag{3.3}$$

$$\boldsymbol{H}(\mathbf{r},t) = Re\{\boldsymbol{H}(\boldsymbol{r})e^{-i\omega t}\} \tag{3.4}$$

In this work, we assume that the materials we consider are non-magnetic, linear, isotropic, and exhibit local optical response. These conditions together lead to the following formulation of Maxwell equations in the frequency domain.

$$\nabla \times \boldsymbol{E} = i\omega\mu_0\boldsymbol{H} \tag{3.5}$$

$$\nabla \times \boldsymbol{H} = -i\omega\epsilon(\mathbf{r},\omega)\epsilon_0\boldsymbol{E} \tag{3.6}$$

$$\epsilon^{-1}\nabla \times \mu^{-1}\nabla \times \boldsymbol{E} - \omega^2\boldsymbol{E} = 0 \tag{3.7}$$

Where $\mu_0 = 4\pi\cdot 10^{-7}\, V\cdot A^{-1}\cdot m^{-1}$ is the permeability in vacuum, $\epsilon(\mathbf{r},\omega) = \epsilon' + i\epsilon''$ is the relative permittivity, ϵ_0 is the dielectric permittivity in vacuum. It is worth explicitly stating the relation between the relative permittivity and the complex refractive index $\epsilon(\mathbf{r},\omega) = n(\mathbf{r},\omega)^2$.

The growing complexity and miniaturisation of nano-optical components make simulations indispensable. As devices approached the scale of a wavelength of light, the rigorous solution of Maxwell's equations became a key to designing optical components, assessing their feasibility, and supporting experimental

results. Many techniques have been employed to solve the electromagnetic problem. FEM is applied to the Maxwell equation to discretise the differential operator. The optical model was numerically solved using the finite element solver JCMsuite [147]. The mesh was constructed such that the maximum side lengths in each material were less than a quarter of the material-dependent wavelength. The basis function polynomial degree was adapted on each element to achieve a target accuracy of under 0.1%. This typically results in polynomial degrees of 3-4 for most elements. The transparent boundary conditions are set using perfectly matched layers. The reflectance and transmittance into the InP substrate were calculated by integrating the outgoing flux density at the top and bottom computational domain boundaries, respectively. The absorptance in each domain was calculated by integrating the electromagnetic field absorption density. The spectral response was calculated in the visible range by varying the wavelength from 410 nm to 980 nm in 10 nm steps. The obtained absorptance was used as the upper limit of the external quantum efficiency (EQE) by assuming that all absorbed photons contribute to the obtained current density, effectively setting the device's internal quantum efficiency to unity. The current density is then given by:

$$J_{ph} = -e \int_{410nm}^{980nm} \frac{A(\lambda)\Phi_{AM1.5g}(\lambda)}{E(\lambda)}\, d\lambda \tag{3.8}$$

Where e is the electron charge, $A(\lambda)$ is the absorptance, $\Phi(\lambda)$ is the AM1.5g solar spectrum and $E(\lambda)$ is the photon energy per wavelength. The current density outside the active layers is calculated to estimate losses due to parasitic absorption.

4 | Processing and Characterization

4.1 NWs solar cell fabrication

The fabrication of III-V nanowire (NW) solar cells is a multi-stage process that converts as-grown NW arrays into electrically isolated devices, as illustrated in Figure 4.1. After growth, the arrays are coated with a conformal SiO_x shell deposited by ALD, typically using TTBS and TMAl precursors to introduce a small Al content (∼0.6%), which improves film density and adhesion. Similar SiO_x shells are widely used in InP-based NW devices due to their ability to suppress surface recombination on the high-aspect-ratio nanowire sidewalls, thereby preserving carrier lifetime and the open-circuit voltage. As highlighted in previous NW device studies, effective sidewall passivation is essential because unpassivated surfaces dominate nonradiative recombination, especially in axial p-i-n junctions where the depletion region extends along a significant portion of the nanowire length. While SiO_x is well-suited for InP NWs, other III-V materials, such as GaInP, may require alternative dielectric passivation layers, e.g., Al_2O_3 or mixed PO_x layers, to achieve optimal interface quality.

To enable lithography and the formation of the top contacts, the NW arrays are embedded in a spin-coated polymer matrix, typically benzocyclobutene (BCB, Cyclotene 3022-46) or S1818. The polymer fills the voids between nanowires, mechanically stabilises the array, and provides a planar surface suitable for photolithography. It reduces the electrical length of the transparent conductive oxide. A controlled reactive-ion etching (RIE) step is used to recess the polymer until the Au catalyst particles are exposed. A second RIE step selectively removes

the SiO_x, exposing the Au catalyst particle.

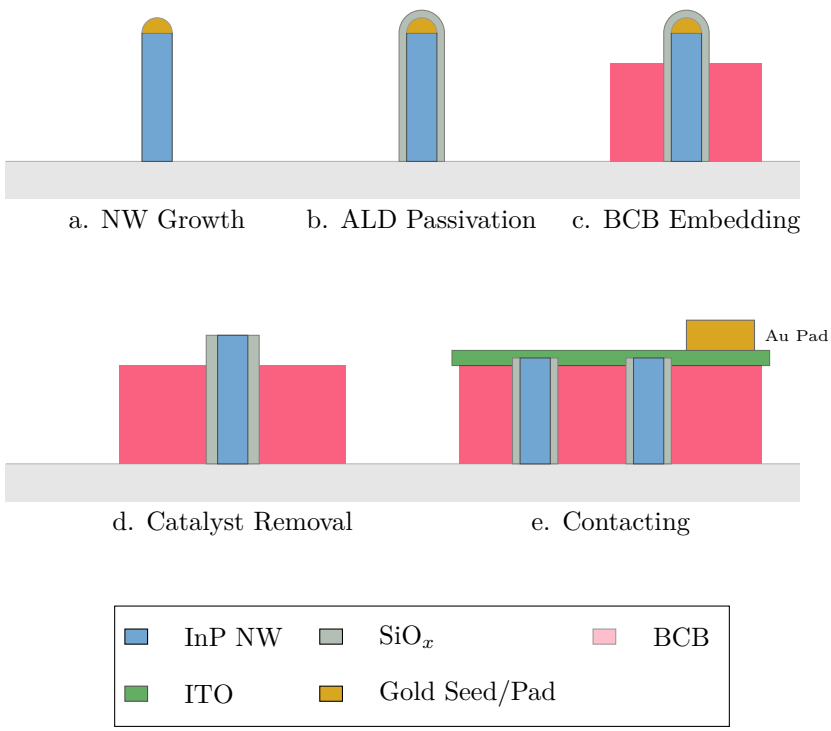

Figure 4.1: Sequence of the NW solar cell fabrication process. (a) As-grown InP NWs on the growth substrate with Au catalyst seeds still present at the tips. (b) Conformal passivation via ALD, depositing a SiO_x shell. (c) Planarization with a spin-coated polymer (BCB), embedding the array to provide structural support for the top contact. (d) Catalyst and oxide removal: RIE etching to recess the BCB and SiO_x, followed by wet etching in H_2SO_4 and KI/I_2 to remove the gold seeds. (e) Device completion: sputtering of the transparent ITO top electrode and final metallization of the Au probe pads.

The Au catalyst particles must be completely removed before device contacting, since residual Au at the nanowire tips acts as an optical reflector, a recombination centre, and a source of parasitic alloying with the SiO_x shell. Incomplete removal can also cause Fermi-level pinning and electrical shunting, which degrade device performance. Removal is carried out using a wet-etch sequence consisting of a brief sulfuric acid dip to dissolve native oxides and prepare the Au interface, followed by KI/I_2 etching to dissolve the metallic Au. Finally, the samples are rinsed in deionised water. Complete seed removal is essential to ensure stable and reproducible ITO-to-NW electrical contacts.

The subsequent lithography steps define the device area (DA), the transparent top electrode, and the metal pads for probing, as illustrated in Figure 4.2. A hard-baked S1828 photoresist frame is patterned around each device, mechanically stabilising the polymer-embedded NW array and electrically isolating adjacent cells. Within the DA, the nanowire tips remain exposed for the formation of the transparent top contact. Indium tin oxide (ITO) is sputtered onto the sample, and an S1813 mask protects selected regions during an HCl-based selective etch that removes ITO between devices. This ensures that each device area contains an isolated parallel-connected ensemble of nanowires. Finally, Ti/Zn/Au pads are defined by lift-off to provide robust and low-resistance probe contacts. The Zn interlayer is included to promote an ohmic contact to p-type InP substrates. This vertical contacting scheme allows millions of nanowires to be connected in parallel while maintaining device-to-device electrical isolation.

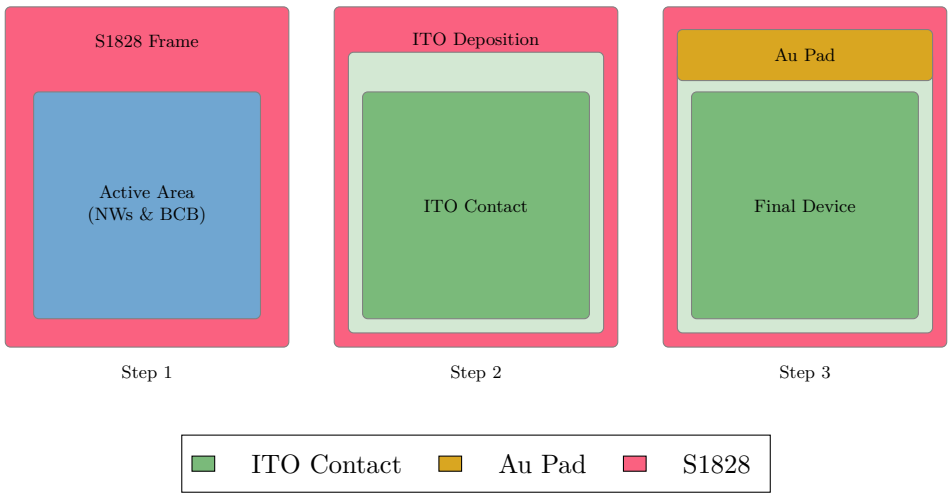

Figure 4.2: Top-down view of the device processing flow. Step 1: Definition of the active area through a hard-baked S1828 photoresist frame. Step 2: Sputtering and selective etching of the ITO transparent conductive oxide. Step 3: Evaporation of the Au bus-bar and probe pads via lift-off process.

4.2 Perovskite deposition

4.2.1 Spin-coating

Spin-coating is the primary method for solution-based thin film deposition. It stands as one of the most commonly employed techniques for perovskite solar cell processing. Firstly, the precursor solution is deployed to the substrate fixed to the spin-coater, generally by vacuum and rotated. The solution excess is removed due to centrifugal force. Film formation depends upon the supersaturation, defined as the ratio between solute concentration and solubility limit. The resulting film thickness is influenced by precursor concentration, solution viscosity, temperature, and spin speed. Processing perovskites by spin-coating requires an understanding of the crystallisation to obtain full coverage and controlled morphology of grains and their boundaries. Despite the advancements obtained through spin-coating, it is not applicable to large-scale manufacturing since 95-98 % is wasted during the spinning process. Moreover, it is difficult to scale up this technique while maintaining the layer uniformity.

4.2.2 Inkjet printing

While spin-coating remains the most used method for perovskite processing. The interest in inkjet printing was fostered by its scalability, allowing for technology transfer to large-area industrial production by increasing the size of the printer and the number of nozzles. This method allows for the precise control of micrometre-scale ink droplet deposition without the need for masks or physical contact. It can achieve notable resolutions, enabling a droplet spacing in tens of micrometres. Moreover, inkjet printing technology can be used across various fields, including display printing, solar cell manufacturing, and sensor production.

Inkjet printing can be classified based on how droplets are formed and released, with continuous inkjet printing (CIP) and drop-on-demand (DOD) inkjet printing being the primary types. In DOD inkjet printing, the release of droplets is controlled by an acoustic pulse, determining the expulsion of ink from a reservoir through a nozzle. The pressure pulse, resulting from the contraction of the chamber, ejects the ink out. Consequently, once ink droplets are formed, they are applied to the substrate. The pressure pulse primarily arises from the mechanical deformation of piezoelectric ceramics or the expansion and rupture of bubbles, depending on the mechanism employed to generate the acoustic pulse. DOD inkjet printing has demonstrated optimal performance, allowing for the precise

formation of individual ink droplets.

Initially designed for small-area devices, this technique was first applied to inkjet-printed perovskite solar cells, exemplified by a 0.16 cm^2 device that achieved a power conversion efficiency of 12.3% [148]. The introduction of novel inks further expanded the capabilities of inkjet printing, leading to the development of triple-cation devices with a power conversion efficiency of 12.9% [149]. Demonstrating the adaptability of this approach, Näsström et al. [29] implemented an algorithm to control ink quantity and a series of printheads for depositing different perovskite compounds with varying bandgaps and halide compositions. This method not only showcases the versatility of inkjet printing but also introduces a rapid investigation technique for diverse compounds, spacings and resolutions, offering potential applications in the fabrication of multi-junction solar cells.

4.2.3 Results: Inkjet printing on NWs solar cells

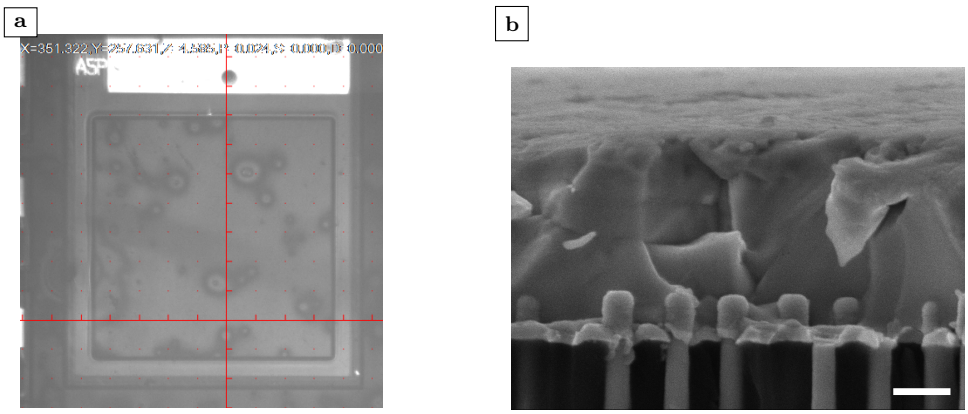

Figure 4.3: Inkjet-printing of $MAPbBr_3$ on NWs solar cell. (a) Capture from the printer camera, the film formation follows the defects of the underlying structure. (b) Cross-sectional view of perovskite printed on the NW bottom cell. Scale bar: 500 nm.

To assess the feasibility of the structure, the bottom cell underwent additional processing with perovskite to assess the solution's penetration between the nanowires (NWs). Employing a PIXDRO LP50 inkjet printer, the experiment utilised a sonicated and filtered solution. Following a 30-minute sonication, the samples underwent ozone treatment for 15 minutes before being transferred to an N_2 glovebox.

The optimisation of nozzle droplet ejection initially focused on achieving a thinner coverage to prevent over-flooding surrounding areas. $MAPbBr_3$ was chosen as

the perovskite for this experiment due to its reported stability [150] and its wide bandgap of approximately 2.25 eV, which makes it a suitable candidate for 3T multijunction solar cells. In this context, its absorption onset at 550 nm simplifies the analysis of the bottom cell. In Figure 4.3, a optical microscope image and a SEM image illustrate the challenge of achieving uniformity in the layer. The perovskite starts crystallising immediately after droplet release, and the device's size (800 µm × 800 µm) imposes limitations on achieving better control over coverage, thereby impacting the resulting thickness.

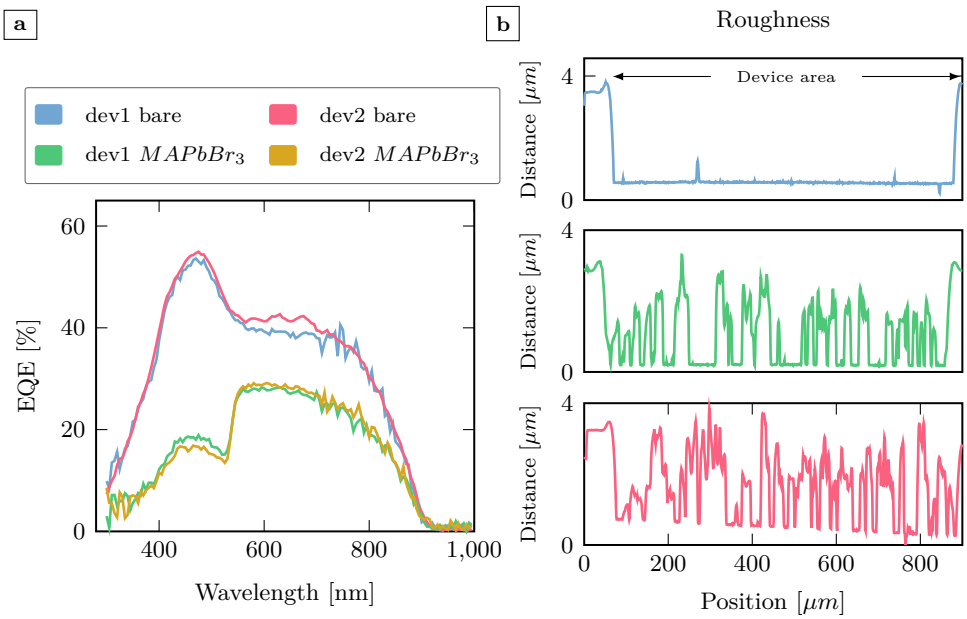

Figure 4.4: (a) EQE of the bottom cell with and without $MAPbBr_3$ on top, the decrease in EQE in the bottom cell follows the light absorption in the perovskite. (b) Roughness measured with a profilometer. The uniformity across the sample is poor.

The external quantum efficiency profile of the bottom cell is depicted in Figure 4.4a. A comparison with the solar cell lacking perovskite on top reveals that the spectrum subtracted from the bare InP solar cell aligns with simulation results. However, the reduction in the spectrum of the bare NWs solar cell for wavelengths beyond 550 nm is more prominent than anticipated by the simulation. This discrepancy can be attributed to increased reflectivity. In the simulation, the reflectivity contribution doubles from 1.5 mA/cm^2 to 3.0 mA/cm^2. This phenomenon is likely exacerbated by the non-uniformity of the layer, as evidenced by the profilometer measurements in Figure 4.4b. The I/V curve presented illustrates a slightly lower V_{OC} and short-circuit current,

attributable to the reduced amount of absorbed light in the bottom cell.

4.2.4 Nanoprobe characterisation of the Tandem solar cell

Multi-junction devices were fabricated using a spin-coating technique, in a similar fashion to Lee and collaborators [151], thus depositing a hydrophobic self-assembled monolayer (SAM) covering the surface outside the bottom cell device area. Figure 4.5 illustrates the device fabrication sequence. Panel (a) shows the steps involved in fabricating the bottom cell, from nanowire growth, as discussed in Section 3.3, to the completed devices, including passivation and the definition of contact areas. The finished bottom cell (Fig. 4.5b) is subsequently coated with a hydrophobic self-assembled monolayer (SAM) and patterned to promote adhesion of the perovskite active layer exclusively on the bottom-cell device area (Fig. 4.5c). Then, perovskite ($MAPbBr_3$) and CuSCN (HTL) are spin-coated, and the top ITO contact is sputtered. The sample is covered with photoresist, which is then developed outside the DA to pattern perovskite, HTL and ITO. In Figure 4.5d, the result of the previous steps is shown with an optical image of the top cell fabrication.

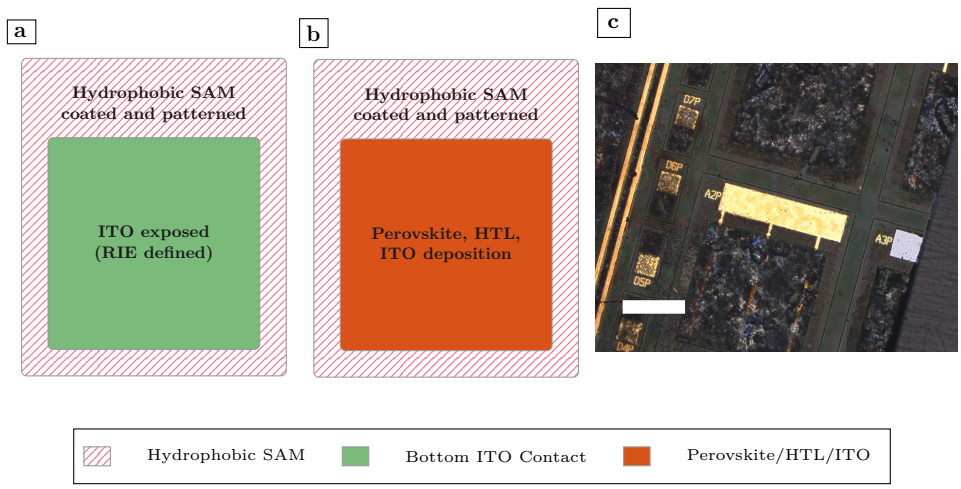

Figure 4.5: Device fabrication. (a) Top view schematic of the bottom cell. (b) On top of the bottom cell device area (DA), perovskite and CuSCN (HTL) are spin-coated, top ITO contact is sputtered. The sample is covered with photoresist, which is then developed outside the DA to pattern perovskite, HTL and ITO. (c) Final tandem device after photoresist stripping using a perovskite-friendly solvent. Scale bar: 400 μm.

Due to adhesion issues and the important observed roughness, it was difficult to measure a full device, so the tandem structure was measured using the setup

detailed in section 3.4.2. In this way, it was possible to inspect an area of interest and contact directly the ITO layer, keeping the contact between subcells.
When scanning with the electron beam, it was possible to obtain a current generation map of the structure (Fig. 4.6a), the lower end value is expected from multi-junction structure, since the current maximum is set by smallest current, and due to the high bandgap of the top cell ~ 2.35 eV. Nanoprobe I/V characteristic under the electron beam illumination (Fig. 4.6b), shows that the V_{OC} is higher than the respective subcells for a total of $V_{OC} = 2.74$V, proving tandem operation, though the FF is small. Though the performances of the device are limited by the roughness of the layers and the quality of the contacts, the demonstration of operation opens up the path for future optimisation.

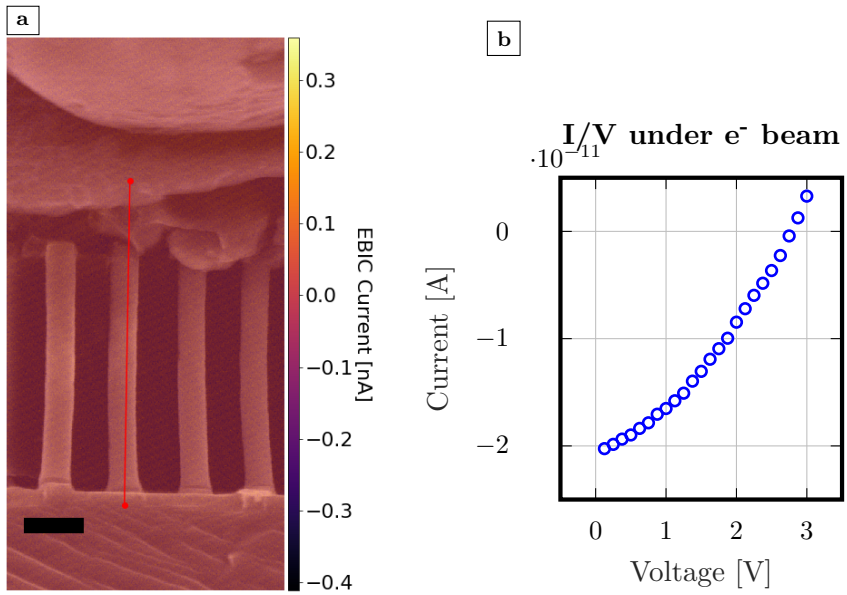

Figure 4.6: Device characterisation of the tandem structure, considering contributions from four NWs. (a) Electron-beam-induced current map of the Tandem cell. Scale bar: 250 nm. (b) I/V under electron beam illumination proving the voltage addition between the subcells and their operation in Tandem junction configuration.

5 | Summary and Results

This thesis is based on the results reported on three complementary studies. Their focus is on the development, characterisation, and modelling of III–V semiconductor nanowires for photovoltaic applications and their integration with perovskite materials. Paper I describes the electrical and structural analysis of vertically processed GaInP/InP tandem junction nanowire solar cells, decoupling the semiconductor material quality, characterised by EBIC measurements, from processing-induced device bottlenecks. In Paper II, nanowires and perovskite/III–V tandem solar cells are investigated using optical modelling to establish the critical layer thicknesses that determine absorptance and reflectance. The model accounts for two-terminal and three-terminal electrical configurations, which require different approaches. The study reported in Paper III is an extensive epitaxy investigation of GaAs nanowire arrays across a broad MOVPE parameter space, aiming to determine the growth conditions that lead to defect-free nanowires.

5.1 Paper I

Nanowires, with their high surface-to-volume ratio, are particularly suitable for tandem solar cells, since they allow integration of lattice-mismatched materials through strain relaxation in the vertical direction and degenerate doping profiles that enable Esaki tunnel diodes, making them electrically and optically transparent and allowing current to flow between the subcells.
This work focuses on the fabrication and characterisation of vertically processed GaInP/InP tandem nanowire solar cells. EBIC measurements were used to evaluate the electrostatic potential profile of single nanowires prior to device

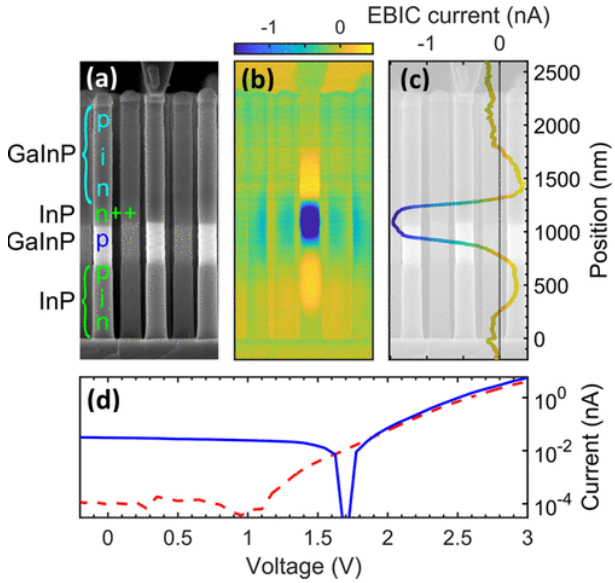

Figure 5.1: SEM and EBIC characterisations GaInP/InP NW. (a) SEM image of an NW contacted with a tip. Annotation shows the position of the bottom InP n–i–p junction, the p-GaInP/n+-InP Esaki tunnel junction, and the top GaInP n–i–p junction. (b) The EBIC image was recorded under a forward bias of 2.8 V. (c) EBIC line profile along the contacted NW, extracted from the image in panel (b). (d) I–V curves for the same NW, recorded in the dark (red dashed line) and under electron beam illumination (blue line). Reproduced from Paper I.

fabrication 5.1, and consequently to determine growth parameters, such as Ga composition, dopant flow and tunnel diode length. These measurements identify the positions of the junctions, the width of the depletion region, and the presence of recombination-active areas, providing detailed insight into the underlying electronic structure of each sample. Within the same setup, I/V measurements were performed under electron-beam illumination, allowing evaluation of V_{OC}, J_{SC}, and FF.

The behaviour observed in EBIC is reflected in the external quantum efficiency (EQE) spectra shown in 5.2. These spectra make it possible to distinguish the contributions of the GaInP top cell and the InP bottom cell by using different light-biasing conditions. The corresponding IV characteristics of the processed tandem devices, presented in Figure S6, demonstrate how the structural and electronic properties inherited from the as-grown nanowires, in particular the Ga composition, affect current matching between the subcells. Despite the low conversion efficiency, this work opens the path to optimisation to achieve efficient tandem nanowire solar cells.

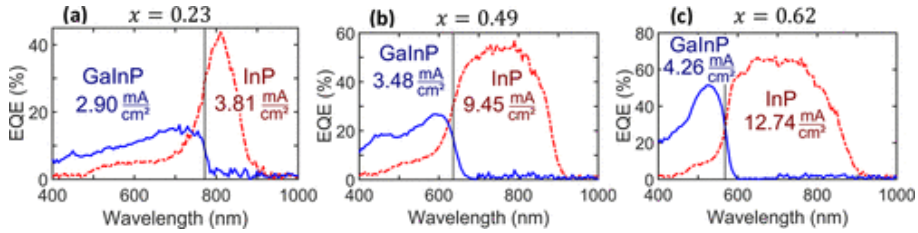

Figure 5.2: EQE characterisation of processed devices for different Ga composition, (a) x=0.23, (b) x=0.49, (c) x=0.62 . The blue curve shows the EQE measurement performed under white light bias, corresponding to the response of the GaInP subcell. The dashed red line shows the EQE measurement under UV light bias, corresponding to the response of the InP subcell. A black vertical line marks the transition between the different subcells where most of the light is absorbed. This occurs at $\lambda = 772\ nm$ for sample (a), $\lambda = 636\ nm$ for sample (b), and $\lambda = 568\ nm$ for sample (c). For each subcell, the theoretically possible generated current density J is indicated, as calculated by integrating the EQE spectrum multiplied by the solar illumination spectrum AM1.5G. Reproduced from Paper I.

5.2 Paper II

In the second work, the finite-element method is employed in optical modelling to investigate the absorption behaviour and loss mechanisms in InP nanowire solar cells and hybrid perovskite/III–V tandems. This work explores both two-terminal (2T) and three-terminal (3T) device architectures, providing a comprehensive understanding of how geometry, material choice, and layer thickness influence the optical performance.

The analysis of the InP nanowire bottom cell begins with an examination of the role of the ITO front contact. Figures 5.3a and 5.3b show that increasing the ITO thickness leads to greater parasitic absorption and shifts the interference pattern of the reflected light. These variations strongly influence the overall absorptance of the nanowire array, highlighting the trade-offs between optical and electrical considerations.

For the 3T tandem configuration, the absorptance is modulated to maximise the total current. The interaction between the perovskite absorber and the nanowire structure is explored by modulating the BCB fill height and the thickness of the perovskite overstanding layer. The perovskite material between the nanowires contributes to the photocurrent and can play a significant role in the spectral distribution of absorption between the two subcells, serving as a tool to tune the electrical response in a multi-junction.

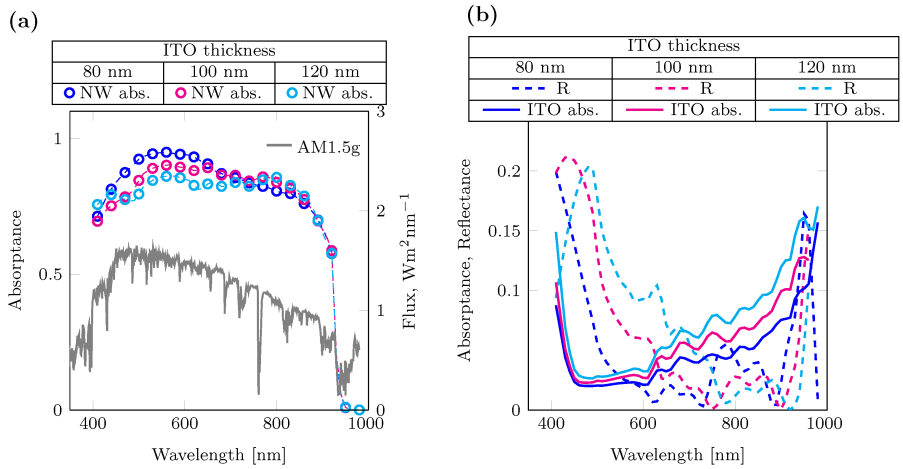

Figure 5.3: Bottom cell optimisation. (a) Calculated absorptance of the bottom InP subcell for different ITO thicknesses (dotted lines), the AM1.5g spectrum is reported (solid grey line). (b) Reflectance (dashed lines) and parasitics contributions for different ITO thicknesses (solid lines). Reproduced from Paper II.

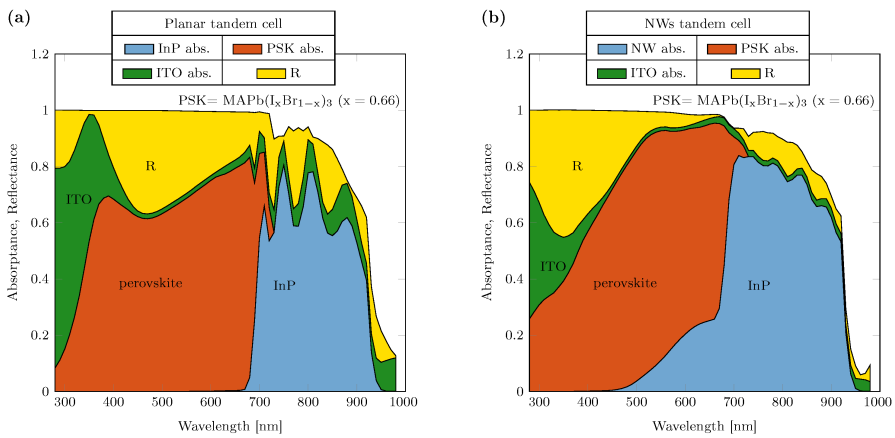

Figure 5.4: Absorptance of 2T devices for (a) planar tandem architecture. The perovskite and InP thicknesses are 1500 nm and 2000 nm, respectively. (b) NW's tandem architecture. Perovskite overstanding layer thickness = 250 nm, InP NWs diameter = 240 nm, length = 2200 nm. Reproduced from Paper II.

When the 2T case is considered, the current matching condition is superimposed; thus, the product between the absorptance and the AM1.5g spectrum is equal. Furthermore, comparing the nanowire-based tandem architecture with the equivalent planar structure, reported in Fig. 5.4, shows that the latter exhibits strong

reflection losses, whereas the nanowire-based tandem benefits from an inherent anti-reflective effect, due to optical modes. However, the transport layers, in particular the HTL, pose a consistent limitation to the performance.
These results demonstrate the significant optical advantages offered by nanowire geometries, which increase absorptance in both the top and bottom absorbers, even though, in this work, the hexagonal pattern and the optical modes forming in s-polarisation are not considered, which can potentially lead to stronger optical confinement.

5.3 Paper III

III-V semiconductors offer a broad choice of direct bandgap materials suitable for optoelectronic applications; among them, GaAs provides high radiative efficiency and enhanced V_{OC}, but its optoelectronic properties require high crystal quality, due to the high surface recombination velocity. In Paper III, MOVPE-grown GaAs NW arrays using metal-organic vapour phase epitaxy are investigated. This work explores a wide parameter space, including variations in temperature, arsine flow, and trimethylgallium flow within the same run, to understand how these parameters influence nanowire morphology, growth rate, and crystal quality, with a specific focus on twin defects.

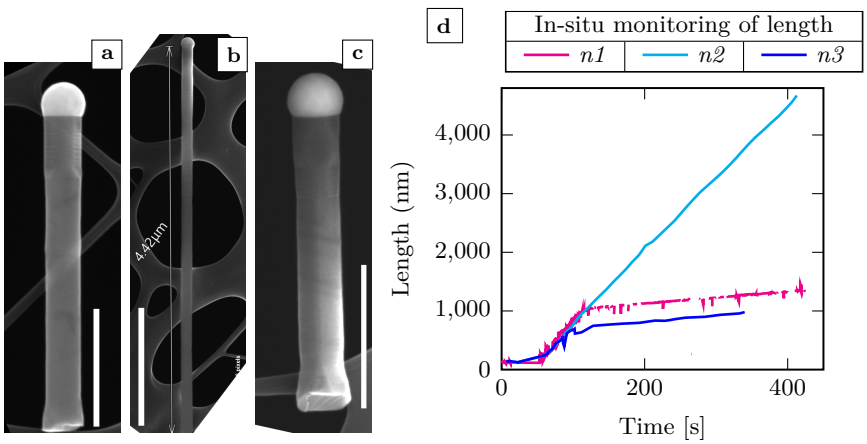

Figure 5.5: SEM images (a),(c), and (c) corresponding to runs *n1*, *n2* and *n3*. These NWs were grown at 400 °C, varying V/III ratio at different AsH_3 and TMGa flows. When the TMGa molar fraction is increased, twin defects form along the NW axis. Scale bar for (a) and (c) is 500 nm and for (b) is 1 μm. (d) Laytec *in situ* reflectometry monitoring of NW length: measurements at early growth do not reflect actual growth due to signal evaluation. Reproduced from Paper III.

Real-time growth dynamics are captured using in-situ optical reflectometry, allowing for time stamps, and linking precursor flow variations to specific locations along the NW axis. These measurements identify transitions between high growth rate conditions, dominated by group-V limitation, and low growth rate conditions associated with Ga supersaturation. Different from previously reported studies, this work focuses on densely packed arrays, which provide an equal amount of material on the entire substrate area with deviations only at the far edges.

SEM images collected across multiple growth runs reveal that dense GaAs nanowire arrays maintain morphological uniformity and straight growth over broad growth conditions. However, when single NWs were inspected in STEM reported in Fig. 5.5, twin defects were observed in Ga rich conditions, in particular at 400 °C, in which case AsH_3 decomposition is incomplete.
In order to deepen the understanding of the obtained results, TEM analysis, presented in Fig. 5.6, provide a detailed view of twin defect formation as a function of the V/III ratio. These images show how catalyst composition and contact-angle modulation influence the appearance and propagation of twins along the nanowire axis. Together, these results define the growth mechanisms responsible for the structural quality of GaAs nanowires and highlight the stability provided by dense array geometries. Photoluminescence spectra indicate that the optical emission, dominated by the uppermost part, depends on the portion of defect-free segments of the nanowires, leading to similar results even when the total nanowire length varies significantly.

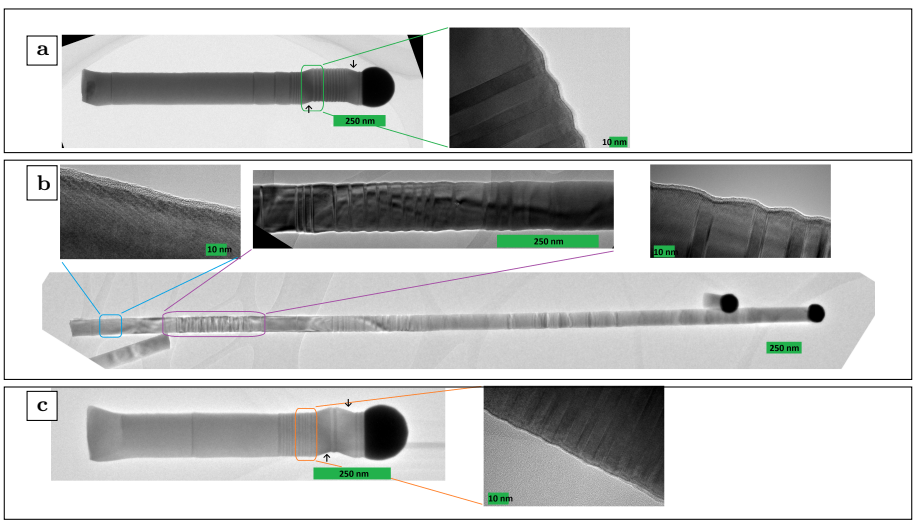

Figure 5.6: TEM images for run *n1* (a), *n2* (b) and *n3* (c), with respective high resolution TEM images. Reproduced from Paper III.

6 | Conclusions and Outlook

6.1 Conclusions

This thesis investigated III–V semiconductor nanowire tandem-junction solar cells and hybrid photovoltaic architectures that combine III–V nanowires with metal–halide perovskites, with the aim of enabling high-efficiency multi-junction devices. Vertically processed GaInP/InP tandem nanowires were demonstrated to operate as intended. EBIC measurements confirmed the correct placement of junctions, the polarity of the tunnel diode, and voltage addition at the single-wire level. The processed devices exhibited open-circuit voltages approaching 2 V. However, the short-circuit current was predominantly limited by the GaInP top sub-cell.

Optical modelling quantified how parasitic absorption in transparent contacts and transport layers constrains the achievable performance. The perovskite material infiltrating the nanowire array also contributes to spectral absorption. It enhances the intrinsic anti-reflection properties of the nanowire geometry. Experimental studies of perovskite deposition on nanowire arrays confirmed the promise of hybrid nanowire–perovskite devices. However, they also underlined the need for controlled nucleation, smooth films, and more sophisticated processing schemes for the transport layers.

Finally, MOVPE growth mapping of GaAs nanowires clarified how precursor conditions influence morphology and defect formation, providing insights relevant for their integration into future multi-junction architectures.

6.2 Outlook

Nanowire surface passivation and contacts

Further reductions in GaInP sidewall recombination are essential for increasing the photocurrent of the top sub-cell. The present SiO_x passivation is effective for InP but remains insufficient for GaInP. Systematic investigations of alternative dielectrics, interfacial chemistries, and refined growth conditions are therefore required. Even small adjustments of the interface V/III ratio have already shown measurable improvements in electronic performance.

GaAs/AlGaAs core–shell structures offer an additional opportunity. AlGaAs provides excellent passivation due to its wider bandgap, favourable band offsets, and good lattice matching. This makes GaAs-based architectures attractive for integration with perovskite top absorbers in multi-junction tandems. However, AlGaAs epitaxy faces substantial challenges arising from deep electronic trap states and rapid surface oxidation at high Al concentrations.

Multi-junction nanowires require an n–i–p growth direction to realise efficient tunnel diodes. Tunnel junctions rely on highly abrupt doping transitions; however, this is difficult to achieve on the p-type side because the high vapour pressure of Zn-based dopants leads to a delayed stabilisation of the Zn partial pressure in the growth chamber, preventing sharp doping transitions. At the same time, transparent conductive oxides such as ITO are intrinsically n-type selective and therefore not optimal for p-terminated structures. Emerging p-selective contacts, such as MoO_x, are promising, but their integration requires modifications to the fabrication scheme, as MoO_x must be protected from oxidation and is highly sensitive to wet etchants, such as HCl. Organic hole-selective layers, such as Spiro-OMeTAD, offer high conductivity but suffer from long-term instability and solvent restrictions.

Integrating inorganic spacers such as SiO_x in place of polymer layers may improve film control, adhesion, and mechanical stability. This could enable applications beyond conventional terrestrial photovoltaics or make perovskite integration easier. Nanowire solar cells currently use thick substrates to define the back contact. Using mechanically robust, stable materials could allow shorter current-collection paths on the front side and improve bonding and device integration. Employing a hard template to facilitate nanowire array peel-off could enable substrate reuse, addressing a key bottleneck in the adoption of III–V materials for terrestrial photovoltaic applications.

Considerations on Hybrid III–V Nanowire and Perovskite processing and modelling

Achieving smooth and conformal perovskite deposition within high-aspect-ratio nanowire arrays requires precise control over wetting, nucleation, and crystallisation. Current deposition approaches frequently produce rough, inhomogeneous films. Such films increase optical reflection and introduce series resistance. Strategies such as solvent-vapour assistance and multi-step crystallisation are promising routes to improve film morphology. Incorporating these advances into optical models will refine the design constraints for two-terminal current matching.

From a modelling perspective, increased computational resources would enable full 3D simulations of the nanowire–perovskite structure. This would allow identification of the specific optical modes responsible for enhanced absorption, including contributions from s-polarised light. It would support systematic optimisation of the hexagonal array pitch and geometry.

The optical analysis also underscores the need to co-design the sheet resistance and optical constants of the transparent front electrode. ITO thickness must be balanced between conductivity, reflection, and parasitic absorption. Introducing alternative transparent conductors or hybrid metal–oxide stacks into the modelling framework will require accurate optical constants, which in turn necessitate dedicated ellipsometry measurements. Experimentally, hybrid device structures that rely exclusively on nanowire-embedded tunnel diodes may yield higher currents by suppressing parasitic recombination at intermediate transport layers. Additionally, anti-reflection coatings such as LiF should be explored both theoretically and experimentally to determine whether they can provide measurable reductions in front-surface reflection.

References

[1] I. E. Agency. *Global Energy Review 2025: Electricity*. 2025. Available at: https://www.iea.org/reports/global-energy-review-2025/electricity.

[2] I. E. Agency. *Renewables 2024: Global Overview*. 2024. Available at: https://www.iea.org/reports/renewables-2024/global-overview.

[3] Ember. *Statistical Review of World Energy - with Major Processing by Our World in Data*. 2025. Available at: https://ourworldindata.org/grapher/share-elec-by-source.

[4] G. L. Barbose et al. Tracking the Sun: Pricing and Design Trends for Distributed Photovoltaic Systems in the United States, 2023 Edition. Report. Lawrence Berkeley National Laboratory, Energy Technologies Area, 2023. Available at: https://emp.lbl.gov/publications/tracking-sun-pricing-and-design-2.

[5] M. A. Green. Commercial Progress and Challenges for Photovoltaics. *Nature Energy* 1.15015 (2016). DOI: 10.1038/nenergy.2015.15.

[6] LONGi Green Energy Technology. LONGi Achieves 27.81% Efficiency for Hybrid Interdigitated Back Contact (HIBC) Silicon Solar Cell. *pv magazine International* (2025). Available at: https://www.pv-magazine.com/2025/04/14/longi-claims-worlds-highest-efficiency-for-silicon-solar-cells/.

[7] LONGi Green Energy Technology. 25.4% Module Efficiency: LONGi Sets New World Record. *LONGi News* (2024). Available at: https://

www.longi.com/eu/news/25-4-module-efficiency-world-record-hpbc/.

[8] W. Shockley and H.-J. Queisser. Detailed Balance Limit of Efficiency of p–n Junction Solar Cells. *Journal of Applied Physics* 32.3 (1961), pp. 510–519. DOI: 10.1063/1.1736034.

[9] L. C. Hirst and N. J. Ekins-Daukes. Fundamental Losses in Solar Cells. *Progress in Photovoltaics: Research and Applications* 19.3 (2011), pp. 286–293. DOI: 10.1002/pip.1024.

[10] A. Polman and H. A. Atwater. Photonic Design Principles for Ultrahigh-Efficiency Photovoltaics. *Nature Materials* 11 (2012), pp. 174–177. DOI: 10.1038/nmat3263.

[11] H. Cotal et al. III–V Multijunction Solar Cells for Concentrating Photovoltaics. *Energy & Environmental Science* 2 (2009), pp. 174–192. DOI: 10.1039/b809257e.

[12] R. M. France et al. Triple-Junction Solar Cells with 39.5% Terrestrial and 34.2% Space Efficiency Enabled by Thick Quantum Well Superlattices. *Joule* 6.5 (2022), pp. 1121–1135. DOI: 10.1016/j.joule.2022.04.024.

[13] NREL. Best Research-Cell Efficiencies (Continuously Updated). *National Renewable Energy Laboratory* (2026). Available at: https://www.nrel.gov/pv/cell-efficiency.html.

[14] *Fraunhofer ISE Develops the World's Most Efficient Solar Cell with 47.6 Percent Efficiency*. 2022. Available at: https://www.ise.fraunhofer.de/en/press-media/press-releases/2022/fraunhofer-ise-develops-the-worlds-most-efficient-solar-cell-with-47-comma-6-percent-efficiency.html.

[15] M. A. Green, A. Ho-Baillie and H. J. Snaith. The Emergence of Perovskite Solar Cells. *Nature Photonics* 8 (2014), pp. 506–514. DOI: 10.1038/nphoton.2014.134.

[16] E. L. Unger et al. Roadmap and Roadblocks for Bandgap Tunability of Metal Halide Perovskites. *Journal of Materials Chemistry A* 5 (2017), pp. 11401–11409. DOI: 10.1039/C7TA00404D.

[17] L. Polavarapu et al. Introduction to Halide Perovskite Optoelectronics. *Nanoscale* 15.37 (2023), pp. 15075–15078. DOI: 10.1039/D3NR90170J.

[18] A. Kojima et al. Organometal Halide Perovskites as Visible-Light Sensitizers for Photovoltaic Cells. *Journal of the American Chemical Society* 131.17 (2009), pp. 6050–6051. DOI: 10.1021/ja809598r.

[19] H.-S. Kim et al. Lead Iodide Perovskite Sensitized All-Solid-State Submicron Thin Film Mesoscopic Solar Cell with Efficiency Exceeding 9%. *Scientific Reports* 2 (2012), p. 591. DOI: 10.1038/srep00591.

[20] J. Burschka et al. Sequential Deposition as a Route to High-Performance Perovskite-Sensitized Solar Cells. *Nature* 499 (2013), pp. 316–319. DOI: 10.1038/nature12340.

[21] S. Jiang et al. Phase Transitions of Formamidinium Lead Iodide Perovskite under Pressure. *Journal of the American Chemical Society* 140.42 (2018), pp. 13952–13957. DOI: 10.1021/jacs.8b09316. Available at: https://doi.org/10.1021/jacs.8b09316.

[22] J. H. Noh et al. Chemical Management for Colorful, Efficient, and Stable Hybrid Perovskite Solar Cells. *Nano Letters* 13.4 (2013), pp. 1764–1769. DOI: 10.1021/nl400349b.

[23] S. Akhil et al. Review on Perovskite Silicon Tandem Solar Cells: Status and Prospects 2T, 3T and 4T for Real World Conditions. *Materials & Design* 211 (2021), p. 110138. DOI: 10.1016/j.matdes.2021.110138.

[24] T. Duong et al. Light and Elevated Temperature Induced Degradation (LeTID) in Perovskite Solar Cells and Development of Stable Semi-Transparent Cells. *Solar Energy Materials and Solar Cells* 188 (2018), pp. 27–36. DOI: 10.1016/j.solmat.2018.08.017.

[25] S. Wieghold et al. Understanding the Effect of Light and Temperature on the Optical Properties and Stability of Mixed-Ion Halide Perovskites. *Journal of Materials Chemistry C: Materials for Optical and Electronic Devices* 8.28 (2020), pp. 9714–9723. DOI: 10.1039/D0TC02103B.

[26] R. Wang et al. A Review of Perovskite Solar Cell Stability. *Advanced Functional Materials* 29.47 (2019), p. 1808843. DOI: 10.1002/adfm.201808843.

[27] D. Cahen, L. Kronik and G. Hodes. Are Defects in Lead-Halide Perovskites Healed, Tolerated, or Both? *ACS Energy Letters* 6.11 (2021), pp. 4108–4114. DOI: 10.1021/acsenergylett.1c01758.

[28] X.-Z. Chen et al. Inkjet-Printed Organic and Perovskite Solar Cells. *Chinese Journal of Polymer Science* 41 (2023), pp. 1169–1197. DOI: 10.1007/s10118-023-2961-z.

[29] H. Näström et al. Combinatorial Inkjet Printing for Compositional Tuning of Perovskite Thin Films. *Journal of Materials Chemistry A* 10 (2022), pp. 4906–4914. DOI: 10.1039/D1TA09494A.

[30] Oxford PV. *Oxford PV Announces First Commercial Sale of Perovskite–Silicon Tandem Modules*. 2024. Available at: https://www.oxfordpv.com/press-releases/oxford-pv-solar-technology-patent.

[31] LONGi Green Energy Technology. *LONGi Breaks World Record: 34.85% Two-Terminal Perovskite–Silicon Tandem Cell*. 2025. Available at: https://www.longi.com/en/news/silicon-perovskite-tandem-solar-cells-new-world-efficiency/.

[32] N. Anttu and H. Q. Xu. Efficient Light Management in Vertical Nanowire Arrays for Photovoltaics. *Optics Express* 21.S3 (2013), A558–A575. DOI: 10.1364/OE.21.00A558.

[33] N. Anttu. Absorption of Light in a Single Vertical Nanowire and a Nanowire Array. *Nanotechnology* 30.10 (2019), p. 104004. DOI: 10.1088/1361-6528/aafa5c.

[34] J. Wallentin et al. InP Nanowire Array Solar Cells Achieving 13.8% Efficiency by Exceeding the Ray Optics Limit. *Science* 339.6123 (2013), pp. 1057–1060. DOI: 10.1126/science.1230969.

[35] M. T. Borgström et al. Nanowires with Promise for Photovoltaics. *IEEE Journal of Selected Topics in Quantum Electronics* 17.4 (2011), pp. 1050–1061. DOI: 10.1109/JSTQE.2010.2102752.

[36] G. Otnes et al. $In_xGa_{1-x}P$ Nanowire Growth Dynamics Strongly Affected by Doping Using Diethylzinc. *Nano Letters* 17.2 (2017), pp. 702–707. DOI: 10.1021/acs.nanolett.6b03795.

[37] D. Alcer et al. Vertically Processed GaInP/InP Tandem-Junction Nanowire Solar Cells. *ACS Applied Nano Materials* 7 (2024), pp. 2352–2358. DOI: 10.1021/acsanm.3c05909.

[38] L. Hrachowina et al. Realization of Axially Defined GaInP/InP/InAsP Triple-Junction Photovoltaic Nanowires for High-Performance Solar Cells. *Materials Today Energy* 27 (2022), p. 101050. DOI: 10.1016/j.mtener.2022.101050. Available at: https://www.sciencedirect.com/science/article/pii/S2468606922001083.

[39] G. Otnes et al. Understanding InP Nanowire Array Solar Cell Performance by Nanoprobe Measurements. *Nano Letters* 18.5 (2018), pp. 3038–3046. DOI: 10.1021/acs.nanolett.8b00749.

[40] Y. Cui et al. Efficiency Enhancement of InP Nanowire Solar Cells by Surface Cleaning. *Nano Letters* 13.9 (2013), pp. 4113–4117. DOI: 10.1021/nl401216y.

[41] L. E. Black et al. Effective Surface Passivation of InP Nanowires by ALD Al_2O_3. *Nano Letters* 17.10 (2017), pp. 6287–6294. DOI: 10.1021/acs.nanolett.7b02797.

[42] L. Watrin et al. Homoepitaxial Growth of Device-Grade GaAs Using Low-Pressure Remote Plasma CVD. *Materials Science in Semiconductor Processing* 186 (2025), p. 109069. DOI: 10.1016/j.mssp.2024.109069.

[43] E. M. Gaddy. Cost Trade between Multijunction, Gallium Arsenide and Silicon Solar Cells. *Progress in Photovoltaics: Research and Applications* 4.2 (1996), pp. 155–161. DOI: .org/10.1002/(SICI)1099-159X(199603/04)4:2<155::AID-PIP128>3.0.CO;2-\#.

[44] J. Schube et al. Mask-and-Plate: Scalable Front Metallization for III–V Tandems. *Scientific Reports* 13 (2023), p. 15745. DOI: 10.1038/s41598-023-42407-4.

[45] M. A. Steiner. III–V PV Cell Core Capability: Final Technical Report. National Renewable Energy Laboratory (NREL), 2023.

[46] A. A. H. Al-Janabi and R. Chtourou. Solvent Annealing for Improved Performance in Perovskite Solar Cells Fabricated by Pulsed Laser Deposition. *Applied Physics A: Materials Science and Processing* 131.10 (2025), p. 799. DOI: 10.1007/s00339-025-08891-3.

[47] Y. Ji et al. Perovskite Photonic Crystal Photoelectric Devices. *Applied Physics Reviews* 9 (2022), p. 041319. DOI: 10.1063/5.0106118.

[48] Y. Chen et al. Optical Analysis of a III–V Nanowire Array on Si Dual-Junction Solar Cell. *Optics Express* 25.S4 (2017), A665–A679. DOI: 10.1364/OE.25.00A665.

[49] C.-t. Sah, R. N. Noyce and W. Shockley. Carrier Generation and Recombination in P-n Junctions and p-n Junction Characteristics. *Proceedings of the IRE* 45.9 (1957), pp. 1228–1243. DOI: 10.1109/JRPROC.1957.278528.

[50] L. Esaki. New Phenomenon in Narrow Germanium P-n Junctions. *Physical Review* 109.2 (Jan. 1958), pp. 603–604. DOI: 10.1103/PhysRev.109.603.

[51] R. N. Hall. Tunnel Diodes. *Nature* 185 (1960), pp. 814–814. Available at: https://api.semanticscholar.org/CorpusID:26672837.

[52] S. M. Sze and K. K. Ng. Physics of Semiconductor Devices. 3rd ed. Hoboken, NJ: John Wiley & Sons, 2006. ISBN: 978-0-471-14323-9. DOI: 10.1002/0470068329.

[53] K. Bertness, D. Friedman and J. Olson. Tunnel Junction Interconnects in GaAs-based Multijunction Solar Cells. *Proceedings of 1994 IEEE 1st World Conference on Photovoltaic Energy Conversion - WCPEC (a Joint*

Conference of PVSC, PVSEC and PSEC). Vol. 2. 1994, 1859–1862 vol.2. DOI: 10.1109/WCPEC.1994.520728.

[54] W. Guter and A. Bett. I–V Characterization of Tunnel Diodes and Multijunction Solar Cells. *IEEE Transactions on Electron Devices* 53.9 (2006), pp. 2216–2222. DOI: 10.1109/TED.2006.881051.

[55] J. M. Gordon et al. Photovoltaic Hysteresis and Its Ramifications for Concentrator Solar Cell Design and Diagnostics. *Applied Physics Letters* 86.7 (Feb. 2005), p. 073508. DOI: 10.1063/1.1862776.

[56] W. E. McMahon et al. A Framework for Comparing the Energy Production of Photovoltaic Modules Using 2-, 3-, and 4-Terminal Tandem Cells. *Sustainable Energy Fuels* 7.2 (2023), pp. 461–470. DOI: 10.1039/D2SE01167K.

[57] E. L. Warren et al. A Taxonomy for Three-Terminal Tandem Solar Cells. *ACS Energy Letters* 5.4 (2020), pp. 1233–1242. DOI: 10.1021/acsenergylett.0c00068.

[58] J. Keil et al. Minimizing Roughness Induced Optical Losses for a Four-Terminal CdTe/Si Tandem Solar Cell. *PRX Energy* 2.2 (May 2023), p. 023004. DOI: 10.1103/PRXEnergy.2.023004. Available at: https://link.aps.org/doi/10.1103/PRXEnergy.2.023004.

[59] G. B. Stringfellow. Organometallic Vapor-Phase Epitaxy: Theory and Practice. 2nd ed. San Diego: Academic Press, 1999. ISBN: 978-0-12-673842-1. DOI: 10.1016/B978-0-12-673842-1.X5000-5.

[60] L. Sun et al. Chemical Vapour Deposition. *Nature Reviews Methods Primers* 1.5 (2021). DOI: 10.1038/s43586-020-00005-y.

[61] C. A. Larsen et al. Decomposition Mechanisms of Trimethylgallium. *Journal of Crystal Growth* 102.1 (1990), pp. 103–116. DOI: 10.1016/0022-0248(90)90891-N.

[62] J. Wallentin et al. Single GaInP Nanowire p-i-n Junctions near the Direct to Indirect Bandgap Crossover Point. *Applied Physics Letters* 100.25 (2012), p. 251103. DOI: 10.1063/1.4729929.

[63] D. Jacobsson et al. Particle-Assisted $Ga_xIn_{1-x}P$ Nanowire Growth for Designed Bandgap Structures. *Nanotechnology* 23.24 (2012), p. 245601. DOI: 10.1088/0957-4484/23/24/245601.

[64] X. Zeng et al. Electrical and optical evaluation of n-type doping in $In_xGa_{1-x}P$ nanowires. *Nanotechnology* 29.25 (2018), p. 255701. DOI: 10.1088/1361-6528/aabaa5.

[65] X. Zeng et al. InP/GaInP Nanowire Tunnel Diodes. *Nano Research* 11 (2018), pp. 2523–2531. DOI: 10.1007/s12274-017-1877-8.

[66] D. Alcer et al. Comparison of Triethylgallium and Trimethylgallium Precursors for GaInP Nanowire Growth. *Physica Status Solidi (B)* 258.2 (2021), p. 2000400. DOI: 10.1002/pssb.202000400.

[67] D. S. Oliveira et al. Interaction between Lamellar Twinning and Catalyst Dynamics in Spontaneous Core-Shell InGaP Nanowires. *Nanoscale* 7.29 (2015), pp. 12722–12727. DOI: 10.1039/C5NR02747K.

[68] C. F. Cerqueira et al. (Ga,In)P Nanowires Grown without Intentional Catalyst. *Journal of Crystal Growth* 431 (2015), pp. 72–78. DOI: 10.1016/j.jcrysgro.2015.08.009.

[69] H. Hakkinen. The gold-sulfur interface at the nanoscale. *Nature Chemistry* 4.6 (2012), pp. 443–455. DOI: 10.1038/nchem.1352.

[70] V. J. Gómez et al. Wafer-Scale Nanofabrication of Sub-100 Nm Arrays by Deep-UV Displacement Talbot Lithography. *Nanotechnology* 31.29 (May 2020), p. 295301. DOI: 10.1088/1361-6528/ab8764.

[71] P. J. P. Chausse et al. Understanding Resolution Limit of Displacement Talbot Lithography. *Optics Express* 27.5 (Mar. 2019), pp. 5918–5930. DOI: 10.1364/OE.27.005918.

[72] H. H. Solak, C. Dais and F. Clube. Displacement Talbot Lithography: A New Method for High-Resolution Patterning of Large Areas. *Optics Express* 19.11 (May 2011), pp. 10686–10691. DOI: 10.1364/OE.19.010686.

[73] P.-M. Coulon et al. Displacement Talbot Lithography for Nano-Engineering of III-nitride Materials. *Microsystems & Nanoengineering* 5.52 (2019). DOI: 10.1038/s41378-019-0101-2.

[74] R. S. Wagner and W. C. Ellis. Vapor-liquid-solid Mechanism of Single Crystal Growth. *Applied Physics Letters* 4.5 (Mar. 1964), pp. 89–90. DOI: 10.1063/1.1753975. eprint: https://pubs.aip.org/aip/apl/article-pdf/4/5/89/18416939/89_1_online.pdf.

[75] E. Givargizov. Fundamental Aspects of VLS Growth. *Journal of Crystal Growth* 31 (1975), pp. 20–30. DOI: 10.1016/0022-0248(75)90105-0.

[76] H. Okamoto and T. B. Massalski. The Au-Si (Gold-Silicon) System. *Bulletin of Alloy Phase Diagrams* 4 (1983), pp. 190–198. DOI: 10.1007/BF02884878.

[77] A. I. Persson et al. Solid-Phase vs. Liquid-Phase Catalyst States in Nanowire Growth. *Nature Materials* 3 (2004), pp. 677–681. DOI: 10.1038/nmat1202.

[78] J. Johansson et al. Mass Transport Model for III–V Nanowire Growth. *Journal of Physical Chemistry B* 109 (2005), pp. 13567–13571. DOI: 10.1021/jp051702j.

[79] H. J. Joyce et al. Phase Perfection in Zinc Blende and Wurtzite III–V Nanowires Using Basic Growth Parameters. *Nano Letters* 10.3 (2010), pp. 908–915. DOI: 10.1021/nl9035418.

[80] S. A. Dayeh, E. T. Yu and D. Wang. III–V Nanowire Growth Mechanism: V/III Ratio and Temperature Effects. *Nano Letters* 7.8 (2007), pp. 2486–2490. DOI: 10.1021/nl0712668.

[81] V. A. Nebol'sin and A. A. Shchetinin. Role of Surface Energy in the Vapor–Liquid–Solid Growth of Silicon. *Inorganic Materials* 39.9 (Sept. 2003), pp. 899–903. DOI: 10.1023/A:1025588601262.

[82] P. Krogstrup et al. Impact of the Liquid Phase Shape on the Structure of III–V Nanowires. *Physical Review Letters* 106.12 (2011), p. 125505. DOI: 10.1103/PhysRevLett.106.125505.

[83] B. A. Wacaser et al. Preferential Interface Nucleation: An Expansion of the VLS Growth Mechanism for Nanowires. *Advanced Materials* 21.2 (2009), pp. 153–165. DOI: 10.1002/adma.200800440.

[84] F. Glas, J.-C. Harmand and G. Patriarche. Why Does Wurtzite Form in Nanowires of III–V Zinc Blende Semiconductors? *Physical Review Letters* 99 (2007), p. 146101. DOI: 10.1103/PhysRevLett.99.146101.

[85] Y.-C. Chou et al. Atomic-Scale Variability and Control of III–V Nanowire Growth Kinetics. *Science* 343.6176 (2014), pp. 281–284. DOI: 10.1126/science.1244623.

[86] C.-Y. Wen et al. Periodically Changing Morphology of the Growth Interface in Si, Ge, and GaP Nanowires. *Physical Review Letters* 107.2 (July 2011), p. 025503. DOI: 10.1103/PhysRevLett.107.025503.

[87] K. A. D. Thelander et al. Control of III–V Nanowire Crystal Structure by Growth Parameter Tuning. *Semiconductor Science and Technology* 25.2 (2010), p. 024009. DOI: 10.1088/0268-1242/25/2/024009.

[88] Y. Kim et al. Influence of Nanowire Density on the Shape and Optical Properties of Ternary InGaAs Nanowires. *Nano Letters* 6.4 (2006), pp. 599–604. DOI: 10.1021/nl052189o.

[89] J. Wu et al. Control of Composition and Morphology in InGaAs Nanowires Grown by Metalorganic Vapor Phase Epitaxy. *Journal of Crystal Growth* 383 (2013), pp. 158–165. DOI: 10.1016/j.jcrysgro.2013.07.038.

[90] K. Hiruma et al. GaAs Free Standing Quantum-size Wires. *Journal of Applied Physics* 74.5 (Sept. 1993), pp. 3162–3171.

[91] K. Hiruma, M. Yazawa, T. Katsuyama et al. Growth and Optical Properties of Nanometer-Scale GaAs and InAs Whiskers. *Journal of Applied Physics* 74 (1993), p. 3162. DOI: 10.1063/1.354907.

[92] D. Reep and S. Ghandhi. Morphology of Organometallic CVD Grown GaAs Epitaxial Layers. *Journal of Crystal Growth* 61.3 (1983), pp. 449–457. DOI: 10.1016/0022-0248(83)90173-2.

[93] A. I. Persson et al. Growth of Vertically Aligned InAs Nanowires on GaAs. *Journal of Crystal Growth* 272 (2004), pp. 167–176. DOI: 10.1016/j.jcrysgro.2004.09.005.

[94] S. A. Kukushkin and N. V. Sibirev. On the Mechanism of the Vapor-Solid-Solid Growth of Au-catalyzed GaAs Nanowires. *Semiconductors* 53.3 (2019), pp. 350–360. DOI: 10.1134/S1063782619030102.

[95] M. Tchernycheva, J.-C. Harmand, G. Patriarche et al. Growth and RHEED Analysis of GaAs Nanowires. *Nanotechnology* 17 (2006), pp. 4025–4030. DOI: 10.1088/0957-4484/17/16/016.

[96] P. Kusch et al. Type-II Band Alignment of Zinc-Blende and Wurtzite Segments in GaAs Nanowires: A Combined Photoluminescence and Resonant Raman Scattering Study. *Physical Review B* 89.4 (Jan. 2014), p. 045310. DOI: 10.1103/PhysRevB.89.045310.

[97] H. J. Joyce et al. Ultralow Surface Recombination Velocity in InP Nanowires Probed by Terahertz Spectroscopy. *Nano Letters* 12.10 (2012), pp. 5325–5330. DOI: 10.1021/nl3026828.

[98] H. J. Joyce et al. Electronic Properties of GaAs, InAs and InP Nanowires Studied by Terahertz Spectroscopy. *Nanotechnology* 24.21 (Apr. 2013), p. 214006. DOI: 10.1088/0957-4484/24/21/214006.

[99] M. T. Borgström et al. In Situ Etching for Total Control over Axial and Radial Nanowire Growth. *Nano Research* 3 (2010), pp. 264–270. DOI: 10.1007/s12274-010-1029-x.

[100] M. T. Borgström et al. Dynamics of Extremely Anisotropic Etching of InP Nanowires by HCl. *Chemical Physics Letters* 502 (2011), pp. 222–224. DOI: 10.1016/j.cplett.2010.12.061.

[101] X. Duan and C. M. Lieber. ChemInform Abstract: General Synthesis of Compound Semiconductor Nanowires. *ChemInform* 31.20 (2000). DOI: 10.1002/chin.200020229.

[102] X. Duan et al. Indium Phosphide Nanowires as Building Blocks for Nanoscale Electronic and Optoelectronic Devices. *Nature* 409.6816 (2001), pp. 66–69. DOI: 10.1038/35051047.

[103] J. Wang et al. Highly Polarized Photoluminescence and Photodetection from Single Indium Phosphide Nanowires. *Science* 293.5534 (2001), pp. 1455–1457. DOI: 10.1126/science.1062340.

[104] T. Mårtensson et al. Nanowire Arrays Defined by Nanoimprint Lithography. *Nano Letters* 4.4 (2004), pp. 699–702. DOI: 10.1021/nl035100s.

[105] S. Bhunia et al. Metalorganic Vapor-Phase Epitaxial Growth and Characterization of Vertical InP Nanowires. *Applied Physics Letters* 83.16 (2003), pp. 3371–3373. DOI: 10.1063/1.1619224.

[106] M. Mattila et al. Crystal-Structure-Dependent Photoluminescence from InP Nanowires. *Nanotechnology* 17.6 (Feb. 2006), p. 1580. DOI: 10.1088/0957-4484/17/6/008.

[107] R. E. Algra et al. Twinning Superlattices in Indium Phosphide Nanowires. *Nature* 456 (2008), pp. 369–372. DOI: 10.1038/nature07570.

[108] S. Lehmann et al. A General Approach for Sharp Crystal Phase Switching in InAs, GaAs, InP, and GaP Nanowires Using Only Group V Flow. *Nano Letters* 13.9 (2013), pp. 4099–4105. DOI: 10.1021/nl401554w.

[109] P. Merle et al. Conduction Band Structure of GaInP. *Physical Review B* 15.4 (Feb. 1977), pp. 2032–2047. DOI: 10.1103/PhysRevB.15.2032.

[110] R. R. King et al. 40% Efficient Metamorphic GaInP-GaInAs-ge Multijunction Solar Cells. *Applied Physics Letters* 90.18 (May 2007), p. 183516. DOI: 10.1063/1.2734507.

[111] M. Yamaguchi et al. Superior Radiation-Resistant Properties of InGaP/GaAs Tandem Solar Cells. *Applied Physics Letters* 70.12 (Mar. 1997), pp. 1566–1568. DOI: 10.1063/1.118618.

[112] M. Hinojosa et al. Improved GaInP/GaAs/GaInAs Inverted Metamorphic Triple-Junction Solar Cells by Reduction of Zn Diffusion in the Top Subcell. *Solar Energy Materials and Solar Cells* 248 (2022), p. 112000. DOI: 10.1016/j.solmat.2022.112000.

[113] S. Assali et al. Direct Band Gap Wurtzite Gallium Phosphide Nanowires. *Nano Letters* 13.4 (2013), pp. 1559–1563. DOI: 10.1021/nl304723c.

[114] Y. Zhao et al. Direct Band Gap White Light Emission from Charge Carrier Diffusion Induced Nanowire Light-Emitting Diodes. *Nano Energy* 132 (2024), p. 110400. DOI: 10.1016/j.nanoen.2024.110400.

[115] K. Adham et al. Characterization of n-doped Branches in Nanotree LEDs. *Energy Adv.* 3.12 (2024), pp. 2922–2928. DOI: 10.1039/D4YA00414K.

[116] J. Johansson and M. Ghasemi. Kinetically Limited Composition of Ternary III-V Nanowires. *Physical Review Materials* 1.4 (Sept. 2017), p. 040401. DOI: 10.1103/PhysRevMaterials.1.040401.

[117] S. Hao et al. Theoretical Prediction and Experimental Confirmation of Unusual Ternary Ordered Semiconductor Compounds in Sr–Pb–S System. *Journal of the American Chemical Society* 136.4 (2014), pp. 1628–1635. DOI: 10.1021/ja411857y.

[118] V. Dubrovskii, A. Koryakin and N. Sibirev. Understanding the Composition of Ternary III-V Nanowires and Axial Nanowire Heterostructures in Nucleation-Limited Regime. *Materials & Design* 132 (2017), pp. 400–408. DOI: 10.1016/j.matdes.2017.07.012.

[119] S. Lehmann et al. High Crystal Quality Wurtzite–Zinc Blende Heterostructures in Metal-Organic Vapor Phase Epitaxy-Grown GaAs Nanowires. *Nano Research* 5 (2012), pp. 470–476. DOI: 10.1007/s12274-012-0232-3.

[120] S. Lehmann, D. Jacobsson and K. A. Dick. Crystal Phase Control in GaAs Nanowires: Opposing Trends in the Ga- and As-limited Growth Regimes. *Nanotechnology* 26.30 (July 2015), p. 301001. DOI: 10.1088/0957-4484/26/30/301001.

[121] D. Jacobsson, S. Lehmann and K. A. Dick. Crystal Structure Tuning in GaAs Nanowires Using HCl. *Nanoscale* 6 (2014), pp. 8257–8264. DOI: 10.1039/c4nr00991f.

[122] Y.-R. Luo. Comprehensive Handbook of Chemical Bond Energies. 1st ed. Boca Raton: CRC Press, 2007. ISBN: 978-0-8493-7366-4. DOI: 10.1201/9781420007282.

[123] S. Irvine and J. Bajaj. A Study of the Growth Kinetics of II–VI Metalorganic Vapour Phase Epitaxy Using in Situ Laser Reflectometry. *Journal of Crystal Growth* 145.1 (1994), pp. 74–81. DOI: 10.1016/0022-0248(94)91031-6.

[124] M. Heurlin et al. In Situ Characterization of Nanowire Dimensions and Growth Dynamics by Optical Reflectance. *Nano Letters* 15.5 (2015), pp. 3597–3602. DOI: 10.1021/acs.nanolett.5b01107.

[125] D. Abou-Ras and T. Kirchartz. Electron-Beam-Induced Current Measurements of Thin-Film Solar Cells. *ACS Applied Energy Materials* 2.8 (2019), pp. 6127–6139. DOI: 10.1021/acsaem.9b01172.

[126] H. J. Leamy. Charge Collection Scanning Electron Microscopy. *Journal of Applied Physics* 53 (1982), R51–R80. DOI: 10.1063/1.331667.

[127] E. Barrigón, L. Hrachowina and M. T. Borgström. Light Current-Voltage Measurements of Single, as-Grown, Nanowire Solar Cells Standing Vertically on a Substrate. *Nano Energy* 78 (2020), p. 105191. DOI: 10.1016/j.nanoen.2020.105191.

[128] L. Hrachowina et al. Imaging the Influence of Oxides on the Electrostatic Potential of Photovoltaic InP Nanowires. *Nano Research* 14.11 (2021), pp. 4087–4092. DOI: 10.1007/s12274-021-3344-9.

[129] E. Barrigón et al. Unravelling Processing Issues of Nanowire-Based Solar Cell Arrays by Use of Electron Beam Induced Current Measurements. *Nano Energy* 71 (2020), p. 104575. DOI: 10.1016/j.nanoen.2020.104575.

[130] L. Hrachowina, E. Barrigón and M. T. Borgström. Development and Characterization of Photovoltaic Tandem-Junction Nanowires Using Electron-Beam-Induced Current Measurements. *Nano Research* 15.9 (2022), pp. 8510–8515. DOI: 10.1007/s12274-022-4469-1.

[131] H. J. Levinson. Principles of Lithography. SPIE Press, 2010.

[132] I. Barbu et al. Advances in Maskless and Mask-Based Optical Lithography on Plastic Flexible Substrates. *Lithography Asia 2009*. Ed. by A. C. Chen et al. Vol. 7520. SPIE / International Society for Optics and Photonics, 2009, 75200A. DOI: 10.1117/12.837171.

[133] Heidelberg Instruments. *MLA 150 Advanced Maskless Aligner*. 2026. Available at: https://heidelberg-instruments.com/product/mla150/.

[134] J. Ai et al. Laser Direct Writing Lithography for Rapid Fabrication on Non-Planar Surfaces. Vol. ICALEO 2017: 36th International Congress on Applications of Lasers & Electro-Optics. Oct. 2017, P151. DOI: 10.2351/1.5138182.

[135] L. Vegard. Die Konstitution Der Mischkristalle Und Die Raumfüllung Der Atome. *Zeitschrift für Physik* 5.1 (1921), pp. 17–26. DOI: 10.1007/BF01349680.

[136] H. F. Zarick et al. Mixed Halide Hybrid Perovskites: A Paradigm Shift in Photovoltaics. *Journal of Material Chemistry A* 6.14 (2018), pp. 5507–5537. DOI: 10.1039/C7TA09122B.

[137] T. J. Jacobsson and A. Hultqvist. An Open-Access Database and Analysis Tool for Perovskite Solar Cells Based on the FAIR Data Principles. *Nature Energy* 7.1 (2022), pp. 107–115. DOI: 10.1038/s41560-021-00941-3.

[138] F. Xu et al. Challenges and Perspectives toward Future Wide-Bandgap Mixed-Halide Perovskite Photovoltaics. *Advanced Energy Materials* 13.13 (2023), p. 2203911. DOI: 10.1002/aenm.202203911.

[139] K. Suchan et al. Complex Evolution of Photoluminescence during Phase Segregation of $MAPb(I_{1-x}Br_x)_3$ Mixed Halide Perovskite. *Journal of Luminescence* 221 (2020), p. 117073. DOI: 10.1016/j.jlumin.2020.117073.

[140] K. Suchan et al. Multi-Stage Phase-Segregation of Mixed Halide Perovskites under Illumination: A Quantitative Comparison of Experimental Observations and Thermodynamic Models. *Advanced Functional Materials* 33.3 (2023), p. 2206047. DOI: 10.1002/adfm.202206047.

[141] C. G. Bischak et al. Tunable Polaron Distortions Control the Extent of Halide Demixing in Lead Halide Perovskites. *The Journal of Physical Chemistry Letters* 9.14 (2018), pp. 3998–4005. DOI: 10.1021/acs.jpclett.8b01512.

[142] Z. Chen et al. Unified Theory for Light-Induced Halide Segregation in Mixed Halide Perovskites. *Nature Communications* 12.2687 (2021), pp. 1–10. DOI: 10.1038/s41467-021-22994-8.

[143] K. Suchan et al. "Light-Induced Halide Vacancies as Key Players in the Temperature-Dependent Phase Segregation of Mixed Metal Halide Perovskites". 2023.

[144] S. Mahesh et al. Revealing the Origin of Voltage Loss in Mixed-Halide Perovskite Solar Cells. *Energy & Environmental Science* 13.1 (2020), pp. 258–267. DOI: 10.1039/C9EE02162K.

[145] G. F. Samu, C. Janáky and P. V. Kamat. A Victim of Halide Ion Segregation. How Light Soaking Affects Solar Cell Performance of Mixed Halide Lead Perovskites. *ACS Energy Letters* 2.8 (2017), pp. 1860–1861. DOI: 10.1021/acsenergylett.7b00589.

[146] M. E. Stuckelberger et al. Effects of X-rays on Perovskite Solar Cells. *The Journal of Physical Chemistry C* 124.33 (2020), pp. 17949–17956. DOI: 10.1021/acs.jpcc.0c04645.

[147] S. Burger et al. JCMsuite: An Adaptive FEM Solver for Precise Simulations in Nano-Optics. *Integrated Photonics and Nanophotonics Research and Applications*. Optica Publishing Group, 2008, ITuE4. DOI: 10.1364/IPNRA.2008.ITuE4.

[148] S.-G. Li et al. Inkjet Printing of $CH_3NH_3PbI_3$ on a Mesoscopic TiO_2 Film for Highly Efficient Perovskite Solar Cells. *Journal of Materials Chemistry A: Materials for Energy and Sustainability* 3.17 (2015), pp. 9092–9097. DOI: 10.1039/C4TA05675B.

[149] F. Mathies et al. Inkjet-Printed Triple Cation Perovskite Solar Cells. *ACS Applied Energy Materials* 1.5 (2018), pp. 1834–1839. DOI: 10.1021/acsaem.8b00222.

[150] L. McGovern et al. Understanding the Stability of MAPbBr3 versus MAPbI3: Suppression of Methylammonium Migration and Reduction of

Halide Migration. *The Journal of Physical Chemistry Letters* 11.17 (2020), pp. 7127–7132. DOI: 10.1021/acs.jpclett.0c01822.

[151] W. Lee et al. High-Resolution Spin-on-Patterning of Perovskite Thin Films for a Multiplexed Image Sensor Array. *Advanced Materials* 29.40 (2017), p. 1702902. DOI: 10.1002/adma.201702902.

Scientific publications

Printed by Media-Tryck, Lund 2026 NORDIC SWAN ECOLABEL 3041 0903

Department of Physics
Faculty of Engineering

ISBN 978-91-8104-988-6